A Harmonic Polynomial Cell (HPC) Method for 3D Laplace Equation with Application in Marine Hydrodynamics

Yan-Lin Shao *, Odd M. Faltinsen

Centre for Autonomous Marine Operations and Systems (AMOS),
Department of Marine Technology, NTNU, NO-7491Trondheim, Norway

Abstract

We propose a new efficient and accurate numerical method based on harmonic polynomials to solve boundary value problems governed by 3D Laplace equation. The computational domain is discretized by overlapping cells. Within each cell, the velocity potential is represented by the linear superposition of a complete set of harmonic polynomials, which are the elementary solutions of Laplace equation. By its definition, the method is named as Harmonic Polynomial Cell (HPC) method. The characteristics of the accuracy and efficiency of the HPC method are demonstrated by studying analytical cases. Comparisons will be made with some other existing boundary element based methods, e.g. Quadratic Boundary Element Method (QBEM) and the Fast Multipole Accelerated QBEM (FMA-QBEM) and a fourth order Finite Difference Method (FDM). To demonstrate the applications of the method, it is applied to some studies relevant for marine hydrodynamics. Sloshing in 3D rectangular tanks, a fully-nonlinear numerical wave tank, fully-nonlinear wave focusing on a semi-circular shoal, and the nonlinear wave diffraction of a bottom-mounted cylinder in regular waves are studied. The comparisons with the experimental results and other numerical results are all in satisfactory agreement, indicating that the present HPC method is a promising method in solving potential-flow problems. The underlying procedure of the HPC method could also be useful in other fields than marine hydrodynamics involved with solving Laplace equation.

Keywords: Harmonic Polynomial Cell (HPC) Method; Laplace equation; Marine hydrodynamics; Fully nonlinear waves; Wave-body interactions

1. Introduction

Laplace equation is a second-order partial differential equation named after Pierre-Simon Laplace who first studied its properties [25]. It plays important roles in different areas, e.g., fluid dynamics, electromagnetism and astronomy. In fluid dynamics, the general theory of solutions to Laplace equation is known as potential-flow theory.

When dealing with potential-flow problems, an efficient and accurate numerical method is important as it is difficult to solve Laplace equation analytically for a general case. This paper addresses the numerical solutions to 3D Laplace equation for the velocity potential. Our study is motivated by the time-domain fully-nonlinear potential-flow wave-structure interactions analysis in marine hydrodynamics. The characteristic dimensions of structures are assumed much larger than the wave amplitudes so that the viscous effects are secondary and may be accounted for empirically. A future objective is to study wave-induced response of ships and other marine structures in different sea states which each has duration of 3-5 hours. The

* Corresponding author. Email address: yanlin.shao@dnvgl.com.
Present address: Ship Hydrodynamics & Stability Section, DNV GL, Veritasveien 1, 1322 Høvik, Norway.

consequence is that large number of time steps is needed. Further, many realizations of each sea state are necessary, in order to obtain reliable predictions of the probability distribution of response variables. Therefore, the efficiency of the Laplace-equation solver to achieve an acceptable accuracy becomes very important.

The numerical methods which can be used to solve Laplace equation may be categorized into two groups. The first group is Boundary Element Methods (BEMs). BEMs solve a boundary integral equation which is a consequence of applying Green's 2nd identity to the Laplace equation. An advantage of BEMs is that one only needs to distribute singularities with unknown strengths on the boundaries of the computational domain. The memory required by a conventional BEM is O(N^2). Here N is the number of unknowns on the boundaries of the computational domain. A direct method such as the Gaussian elimination or LU-factorization takes O(N^3) operations in order to solve the resulting matrix equation. Typical iterative solvers, e.g. the Gauss-Seidel method and the Krylov subspace Generalized Minimal Residual method (GMRES), would yield O(N^2) operation counts and consequently O(N^2) CPU time. Therefore, both CPU time and required memory for conventional BEM increase dramatically with increasing number of unknowns, which was considered as the bottleneck of the conventional BEMs. Recent developments in BEMs showed that the bottleneck no longer exists if the accelerated methods, e.g. the pre-corrected Fast Fourier Transform (*p*-FFT) method [22, 23] and the fast multipole accelerated (FMA) method [14, 27, 43], are combined with the BEM solvers. Asymptotically, the *p*-FFT method needs O(Nlog$N$) memory and O(Nlog$N$) CPU time, and the newer version of FMA needs O(N) memory and O(N) CPU time.

The other group includes field solvers, which needs to discretize the whole computational domain. Examples are Finite Element Method (FEM), Finite Difference Method (FDM) and Finite Volume Method (FVM). One of the advantages of field methods is that one operates with sparse matrices, which can be solved very efficiently. Wu & Eatock Taylor [53] suggested that the 2D Finite Element Method field solver is much more efficient than their conventional BEM in terms of both CPU time and computer memory by studying a fully-nonlinear numerical wave tank. Their work has been extended to 3D by Ma et al. [32, 33]. Recently, Bingham and Zhang [1] and Engsig-Karup et al. [7, 8] developed an efficient flexible order FDM to model the nonlinear water waves.

In this paper, a new field method based on harmonic polynomials of different orders is designed to solve 3D Laplace equation. A harmonic polynomial satisfies Laplace equation. The basic idea of using the harmonic polynomials to represent the velocity potential in fluid dynamics was first introduced by Euler [9] about 300 years ago. The harmonic polynomials have also been used in solving sloshing of liquids in tanks [31], where the harmonic polynomials are used globally in the whole interior fluid domain. The boundary conditions are then enforced and the approximation of the solution is found by variational principles. Kennedy & Fenton [20] developed a 2D local polynomial approximation (LPA) method in order to simulate wave propagation over bottom topography. In the LPA method, the fluid domain is divided into multi domains by vertical cuts. 2D harmonic polynomials were used to represent the velocity potential within each domain. The continuity is enforced at the common boundaries of the neighboring domains. The model was shown to be very accurate and efficient in modeling non-breaking nonlinear waves over bottom topography. It is not clear if it is straightforward to apply the LPA method in a general wave body interaction problem. Kennedy & Fenton [19] also extended the idea of local polynomial expansion to 3D problems. However, ordinary polynomials are used instead of harmonic polynomials. Yuldashev & Yuldasheva [56] proposed a new class of 3D finite elements based on harmonic basis functions. It was shown that with fewer nodes on the finite elements, the harmonic polynomials based finite elements can achieve higher accuracy in comparison with the usual Lagrange finite elements.

Keeping the application of general potential-flow wave-body interaction problems in mind, Shao & Faltinsen [46] has proposed a higher-order Harmonic Polynomial Cell (HPC) method in 2D. The computational domain was discretized by overlapping quadrilateral cells. Within each cell, the velocity potential is represented by the linear superposition of a set of harmonic polynomials. Similar to other field methods, the HPC method operates with a sparse matrix which can be solved by any efficient matrix solvers. The HPC method was used to simulate the fully-nonlinear wave propagation over both flat and uneven tank bottoms, showing encouragingly good agreement with the experimental results. Their linear time-domain results for a semi-circle were also in good agreement with the analytical results and the numerical results based on a frequency-domain BEM. They demonstrated the accuracy and efficiency of the HPC method by comparing with a constant BEM, a fast multipole accelerated constant BEM, a second-order accurate finite volume method and a second-order accurate cell method based on Lagrange polynomials. With the number of unknowns which is typical in marine hydrodynamics and considering the CPU time to achieve the same accuracy, it was shown that the HPC method was clearly the fastest among the five methods in the above comparative study.

In this paper, a 3D HPC method is developed, which can be considered as an extension of the work by Shao & Faltinsen [46] in 2D. The paper is organized as follows: In section 2, the derivation of 3D harmonic polynomials in Cartesian coordinate system is briefly shown. Section 3 illustrates the details of the 3D HPC method. In section 4, the method is applied to study a mixed Dirichlet-Neumann boundary value problem on a cube. Comparison will be made with an existing Quadratic Boundary Element Method (QBEM) and a Fast Multipole Accelerated QBEM (FMA-QBEM) by studying a Boundary Value Problem (BVP) on a unit cube with analytical solution. A BVP on a shoe box which was earlier studied by *p*-FFT accelerated QBEM and Fast Multipole Accelerated Cubic BEM (FMA-CBEM) is also revisited. Another Dirichlet-to-Neumann problem with analytical solution is also studied in order to make comparison with a 4th order FDM. Section 5 presents some more applications in marine hydrodynamics including: sloshing in 3D rectangular tanks, a fully-nonlinear numerical wave tank, nonlinear wave focusing on a semi-circular shoal, and the nonlinear wave diffraction of a bottom-mounted free-surface piercing circular cylinder in regular waves.

2. Definition of harmonic polynomials in 3D

In this section, we will briefly show the derivation of 3D harmonic polynomials in the Cartesian coordinate system $Oxyz$. More details can be found in Lukovsky *et al.* [31]. The following presentation is based on a translation of Lukovsky *et al.* [31] from Russian to English by Timokha (personal communication, 2012). Classical definition of 3D harmonic polynomials starts from spherical harmonics, which appear as solution of the 3D Laplace equation in the spherical coordinate system. The relation between the spherical coordinates R,θ,φ and the Cartesian coordinates are

$$x = R\cos\theta,\ z = R\cos\varphi\sin\theta,\ y = R\sin\varphi\sin\theta. \tag{1}$$

Generally speaking, there exist four types of independent solutions following from using separation of variables in solving the Laplace equation, i.e.

$$\boxed{R^n P_n^m(\mu)\begin{matrix}\cos m\varphi\\ \sin m\varphi\end{matrix}},\quad R^{-n-1}P_n^m(\mu)\begin{matrix}\cos m\varphi\\ \sin m\varphi\end{matrix},\quad R^n Q_n^m(\mu)\begin{matrix}\cos m\varphi\\ \sin m\varphi\end{matrix},\ \text{and}\quad R^{-n-1}Q_n^m(\mu)\begin{matrix}\cos m\varphi\\ \sin m\varphi\end{matrix}, \tag{2}$$

where $\mu = \cos\theta$. Further, P_n^m and Q_n^m are the associated Legendre polynomials of the first and second kinds, respectively. If a 3D domain Q is star-shaped relative to the origin O, the first set is only needed due to the fact that the three other sets are singular in Q. The first set is then complete from the mathematical point of view.

See e.g. Vekua [40, 41]. As long as *Q* is not star-shaped relative to *O*, the first set is not complete and we should think on adding other sets. Let us think in term of a sphere *Q* and the origin *O* inside of the sphere (not necessarily the sphere center but inside). In this case, *Q* is star-shaped, and we can take only the first set. As long as the origin *O* is outside of the sphere, the first set is not complete and we must add others, singular sets to get the completeness. In other words, the completeness depends on the coordinate system position in the space.

To define the 3D harmonic polynomials, our focus is on the framed component in Eq. (2) with $n = 0,1,...;\ m = 0,...,n$, where

$$P_0^0(\mu) = 1, \quad P_n^0(\mu) = \frac{1}{2^n n!}\frac{d^n}{d\mu^n}\left[\ \mu^2 - 1\ \right]; \quad P_n^m(\mu) = (1-\mu^2)^{m/2}\frac{d^m}{d\mu^m}P_n^0(\mu)\,. \tag{3}$$

For any fixed number n, we should change m from 0 to n and, as a result, we obtain $2n+1$ different polynomials of the order n. Normally, these polynomials are denoted as

$$C_n^m = b_{nm}R^n P_n^m(\cos\theta)\cos m\varphi \quad \text{and} \quad S_n^m = b_{nm}R^n P_n^m(\cos\theta)\sin m\varphi, \tag{4}$$

where

$$b_{nm} = \frac{2^m m!(n-m)!}{(m+n)!}, \quad \text{and} \quad n = 0,1,...;\ m = 0,1,...,n. \tag{5}$$

Direct derivations give the examples in Cartesian coordinates:

$$n = 0: \quad S_0^0 = 0, \quad C_0^0 = 1; \tag{6}$$

$$n = 1: \quad C_1^0 = x,\ C_1^1 = y,\ S_1^1 = z; \tag{7}$$

$$n = 2: \quad C_2^0 = x^2 - \tfrac{1}{2}(y^2 + z^2), \quad C_2^1 = xy, \quad C_2^2 = y^2 - z^2,\ S_2^1 = xz, \quad S_2^2 = 2yz; \tag{8}$$

$$\begin{aligned} n = 3: \quad & C_3^0 = x^3 - \tfrac{3}{2}\left[xy^2 + xz^2\right], \quad C_3^1 = x^2y - \tfrac{1}{4}y(y^2+z^2), \quad C_3^2 = x(y^2-z^2), \\ & C_3^3 = y(y^2 - 3z^2), \quad S_3^1 = x^2z - \tfrac{1}{4}z(y^2+z^2),\ S_3^2 = 2xyz, \quad S_3^3 = z(3y^2 - z^2) \end{aligned} \tag{9}$$

The following recursive formulas can be used to calculate the harmonic polynomials and their derivatives of any other order

$$\begin{aligned} C_n^m &= \frac{4m(m-1)}{(n-m+1)(n+m)r^2}\left[yC_n^{m-1} - zS_n^{m-1}\right]x - (y^2-z^2)C_n^{m-2} + 2yzS_n^{m-2}\ , \\ S_n^m &= \frac{4m(m-1)}{(n-m+1)(n+m)r^2}\left[yS_n^{m-1} + zC_n^{m-1}\right]x - (y^2-z^2)S_n^{m-2} - 2yzS_n^{m-2}\ , \end{aligned} \tag{10}$$

$$\begin{aligned} C_n^{m+1} &= \frac{2(m+1)}{(n+m+1)r^2}\left[-xC_n^m + R^2C_{n-1}^m\right]y - \left[-xS_n^m + R^2S_{n-1}^m\right]z\ , \\ S_n^{m+1} &= \frac{2(m+1)}{(n+m+1)r^2}\left[-xS_n^m + R^2S_{n-1}^m\right]y + \left[-xC_n^m + R^2C_{n-1}^m\right]z\ , \end{aligned} \tag{11}$$

$$
\begin{aligned}
C_{n+1}^m &= \frac{1}{n+m+1}\left[(2n+1)xC_n^m - (n-m)R^2C_{n-1}^m\right],\\
S_{n+1}^m &= \frac{1}{n+m+1}\left[(2n+1)xS_n^m - (n-m)R^2S_{n-1}^m\right],
\end{aligned}
\tag{12}
$$

$$
\begin{aligned}
&\frac{\partial C_n^m}{\partial x} = (n-m)C_{n-1}^m; \qquad \frac{\partial S_n^m}{\partial x} = (n-m)S_{n-1}^m,\\
&\frac{\partial C_n^m}{\partial y} = \frac{y}{r^2}\left[nC_n^m - (n-m)xC_{n-1}^m\right] + \frac{z}{r^2}mS_n^m,\\
&\frac{\partial C_n^m}{\partial z} = \frac{z}{r^2}\left[nC_n^m - (n-m)xC_{n-1}^m\right] - \frac{y}{r^2}mS_n^m,\\
&\frac{\partial S_n^m}{\partial y} = \frac{y}{r^2}\left[nS_n^m - (n-m)xS_{n-1}^m\right] - \frac{z}{r^2}mC_n^m,\\
&\frac{\partial S_n^m}{\partial z} = \frac{z}{r^2}\left[nS_n^m - (n-m)xS_{n-1}^m\right] + \frac{y}{r^2}mC_n^m.
\end{aligned}
\tag{13}
$$

Here, $r = \sqrt{y^2+z^2}$ and $R = \sqrt{x^2+y^2+z^2}$. It is possible for a given order n to construct other harmonic polynomials. However, since the presented sets of polynomial are complete, other polynomials of a given order n are linear combinations of the above listed polynomials and are therefore not needed.

3. Harmonic polynomial cell (HPC) method in 3D

3.1 Velocity potential interpolation by a set of harmonic polynomials

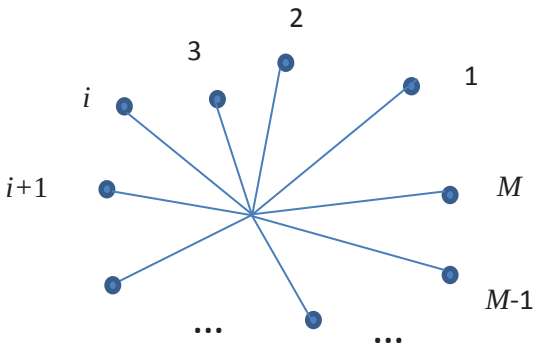

Fig.1. A set of points where the velocity potentials are known.

Considering that the velocity potentials on a set of nodes are known as ϕ_i (i=1,…,M), one can approximate the velocity potential field through interpolation by a set of basis functions. Fig.1 shows an example of M nodes close to each other. In order to approximately interpolate the velocity potential on locations other than these M nodes, one may use, for instance, Lagrange polynomials, which however do not guarantee that Laplace equation is satisfied. Alternatively, the harmonic polynomials discussed in Section 2 can be used as the basis functions for interpolation. We write the velocity potential as the linear combination of a set of harmonic polynomials

$$\phi(x,y,z)=\sum_{j=1}^{N} b_j f_j(x,y,z), \tag{14}$$

where N is the total number of harmonic polynomials used in the interpolation. b_j (j=1,…,N) are the unknown coefficients, which need to be determined. Plugging $\phi=\phi_i$, $x=x_i$, $y=y_i$ and $z=z_i$ (i=1,...,M) into Eq.(14), we get the following equation system

$$\left[\mathbf{M}\right]_{M\times N}\left\{\mathbf{B}\right\}_N=\left\{\Phi\right\}_M, \quad M\le N. \tag{15}$$

Here x_i , y_i and z_i are the x-, y-, and z-coordinates, respectively. The elements of matrix $\left[\mathbf{M}\right]_{M\times N}$ are defined as $m_{i,j}=f_j(x_i,y_i,z_i)$ with i=1,…,M and j=1,…,N. The elements of vector $\left\{\mathbf{B}\right\}_N$ and $\left\{\Phi\right\}_N$ are b_j (j=1,…,N) and ϕ_i (i=1,…,N), respectively. When $\left\{\mathbf{B}\right\}_N$ is solved by Eq.(15), the velocity potential at any location can be approximated by Eq.(14), while the velocities are approximated by differentiating Eq.(14) with respect to x, y and z.

It is most natural to choose the N harmonic polynomials (see C_n^m and S_n^m with $n\ge 0$ and $m\le n$ defined in Section 2) from lower order to higher order. If N is smaller than M, one can solve Eq. (15) in a least-square sense. However, in case of M=N, the equation system (15) is not always solvable when the harmonic polynomials f_j (j=1,…,N) are chosen as the first N lowest harmonic polynomials from C_n^m and S_n^m. In this case, we follow the algorithm proposed by Yuldashev & Yuldasheva [56]:

(1) Define a sequence of functions g_j , $j\ge 1$ as follows:

$$g_1=C_0^0;\ g_2=C_1^0;\ g_3=C_1^1;\ g_4=S_1^1;\ g_5=C_2^0;g_6=C_2^1;g_7=S_2^1;\ g_8=C_2^2;g_9=S_2^2;\ g_{10}=C_3^0;$$

$$g_{11}=C_3^1;\ g_{12}=S_3^1;g_{13}=C_3^2;\ g_{14}=S_3^2;\ g_{15}=C_3^3;g_{16}=S_3^3;\ \ldots \tag{16}$$

Here C_i^j ($i\ge 0$, $j\le i$) and S_i^j ($i\ge 1$, $j<i$) are defined in Section 2.

(2) Construct a standard linear cell by the 8 corner nodes (i.e. nodes 1, 3, 7, 9, 18, 20, 24, 26 in Fig.2) and the set of harmonic polynomials $\{f_1, f_2, f_3, f_4, f_5, f_6, f_7, f_8\}=\{g_1, g_2, g_3, g_4, g_6, g_7, g_9, g_{14}\}$. One can easily repeat a similar procedure to that given in Eq.(14) -Eq.(15) and confirm that the selected set of polynomials results in a solvable system of Eq.(15). Set k=8 and m=4.

(3) If k>N, the set of N harmonic basis functions are formed with the given set of N nodes. Otherwise, add a node with number k to the existing nodes set.

(4) Add a harmonic polynomial $f_{k+1}=g_{m+1}$ to the existing basis function set. g_{m+1} should not be contained in the existing set.

(5) Check the solvability of Eq.(15).

(6) If the system is solvable, set k=k+1 and m=m+1 and go to step 3. Otherwise, set m=m+1 and go to step 4.

3.2 The Harmonic Polynomial Cell (HPC) method

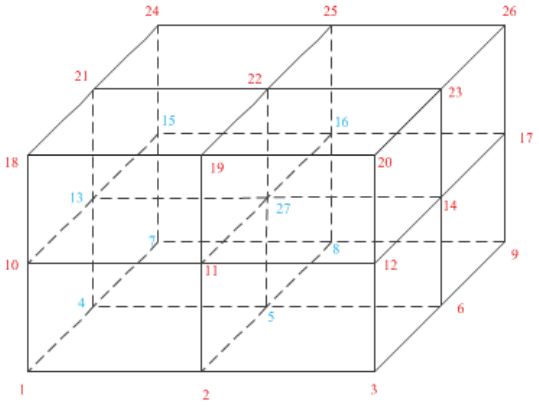

Fig.2. Definition of the local index for a cell centered at grid point (*i*, *j*, *k*) indicated as point 27 in the figure.

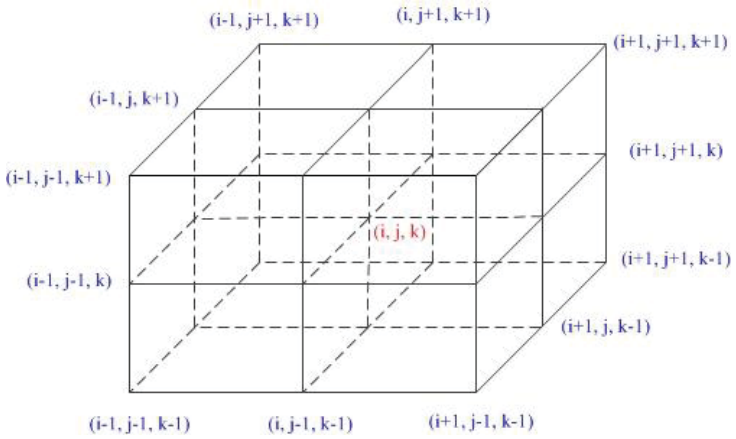

Fig.3. An example of a harmonic polynomial cell containing 8 hexahedrons elements.

In the present HPC method, the water domain is first divided into structured hexahedrons elements. Then we operate with cells that contain 8 neighboring hexahedron elements and 27 grid points. An example of a cell centered at grid point (i, j, k) is shown in Fig.3, where i, j and k are the index of the grid point in *x*-, *y*- and *z*-directions respectively. The local index of the grid points on the cell is defined in Fig.2, with the first 26 nodes on boundaries and the 27th node inside the cell. We use the 26 boundary nodes of the cell and set *M*=*N*=26 in Section 3.1 to approximate the velocity potential within the cell. The procedure listed in step 1-6 gives the following 26 harmonic basis functions

$$\{f_1,\cdots,f_{26}\}=\{g_1,\cdots,g_{21},g_{24},g_{26},\cdots,g_{28},g_{31}\}\ , \tag{17}$$

where g_j ($j\geq 1$) has been defined in Eq.(16). The exact expressions for f_j (j=1,…,26) are also provided in the Appendix. The 26 harmonic polynomials contain all the terms up to 3rd order and some other higher-order terms. It is therefore expected that the present HPC method has approximately 3rd order accuracy.

Let us denote the solution of Eq. (15) with *M*=*N*=26 as

$$b_i = \sum_{j=1}^{26} c_{i,j}\phi_j \ , \ \ i=1,...,26, \tag{18}$$

where $c_{i,j}$ (i, j=1,...,26) is the element of the inverse of the matrix $[\mathbf{M}]_{26\times 26}$. Since the interior 27th node is a boundary node of a neighboring cell, the information for the 27th node of the cell will be used by the neighboring cells in constructing the interpolation functions. For example, a grid point (i, j, k) in Fig.3 is the interior point of the cell centered at (i, j, k), while it is also the 13th boundary node of the neighbor cell centered at point (i+1, j, k).

When b_j (j=1,...,26) is expressed by the linear combination of ϕ_j (j=1,...,26) in Eq.(18), Eq.(14) can be rewritten as

$$\phi(x,y) = \sum_{i=1}^{26}\left[\sum_{j=1}^{26} c_{j,i} f_j(x,y)\right]\phi_i . \tag{19}$$

Therefore, the velocity potential in a cell can be interpolated by only the velocity potential at the boundary nodes of the cell. For simplicity, we assume the origin of the coordinate system has the same location as point 27 of a cell. Considering $(x,y,z) = (x_{27}, y_{27}, z_{27}) = (0,0,0)$, $f_1(0,0,0) = 1$ and $f_i(0,0,0) = 0$ for i >1, the velocity potential on point 27 simplifies as the following single summation

$$\phi\left(x = x_{27} = 0, y = y_{27} = 0, z = z_{27} = 0\right) = \sum_{i=1}^{26} c_{1,i}\phi_i \tag{20}$$

The following equation is then enforced on the 27th points of all the cells

$$\phi_{27} = \phi\left(x = x_{27} = 0, y = y_{27} = 0, z = z_{27} = 0\right) = \sum_{i=1}^{26} c_{1,i}\phi_i \ , \tag{21}$$

which provides the continuity of the flow.

The point 27 shown in Fig.2 is only an example of the grid points away from the boundaries. One can repeat Eq. (21) for all the grid points in the fluid. For points on Neumann boundaries, the boundary conditions are enforced by analytically taking the normal derivative of Eq. (19) at the boundary nodes, i.e.

$$\frac{\partial\phi}{\partial n}(x,y,z) = \sum_{i=1}^{26}\left[\sum_{j=1}^{26} c_{j,i}\nabla f_j(x,y,z)\cdot\vec{n}(x,y,z)\right]\phi_i . \tag{22}$$

Here $\vec{n}$ is the normal vector on the boundary nodes. On Dirichlet boundaries, the velocity potentials are known. Applying the continuity constraints given in Eq. (21) and the boundary conditions, we obtain a global matrix linear algebraic equation with a sparse matrix. The matrix has at most 27 non-zeros in each row. The linear algebraic equation is solved by the generalized minimal residual method (GMRES) solver [44]. A proper preconditioner is very important for an iterative solver to achieve fast convergence. In this article, the ILUT factorization available in Intel Math Kernel Library (MKL) is adopted for the preconditioning. However, there might be better choices of the preconditioner for the present HPC method rather than the ILUT, which will need further investigation in the future.

The derivation of the 26 harmonic polynomials shown in this section is based on cells with grid points on a Cartesian hexahedron. For a highly distorted cell, it is possible that Eq. (15) may not be solvable. Numerical tests using stretched cells indicate that it does not pose a problem from a practical point of view. Even though the boundary of the cells becomes non-star shaped due to distortion, the equation systems were seen to be still solvable as long as a stencil node does not coincide with another stencil node.

Since the present HPC method uses only the non-singular harmonic polynomials in constructing the harmonic polynomial cells, one cannot accurately describe the effect of flow singularities near a sharp corner of a body. Recently, Faltinsen and Timokha [11] used both the regular and singular sets of the harmonic polynomials in an approximate Trefftz solution of the two dimensional natural sloshing problem in two-dimensional tanks with non-vertical tank walls at the mean free surface. Since linearized free-surface conditions are used, there are singularities in the second derivatives of the velocity potential at the intersections between the mean free surface and the non-vertical tank walls. The consequence is bad convergence at the intersections if only the regular harmonic polynomials are used. The singular sets are local solutions at the intersection between the mean free surface and the body surface. Similar idea may be applied in the HPC method. However, this needs an additional study.

4. Accuracy, efficiency and convergence study

4.1 A study on a unit cube

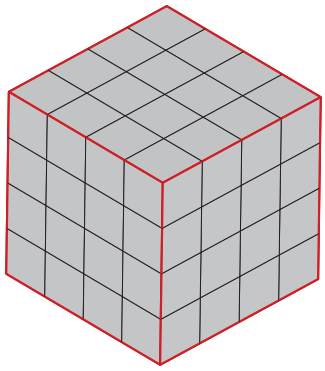

Fig.4. Discretization of a cube with top surface as a Dirichlet surface and the rest as Neumann surfaces.

In order to examine the accuracy and efficiency of the present HPC method, a mixed Dirichlet-Neumann Boundary Value Problem (BVP) on a unit cube (see Fig.4) is studied. The mixed Dirichlet-Neumann BVPs are important elements in the time-domain wave-body interaction problems. The top surface of the cube is set as the Dirichlet surface and the rest as the Neumann boundaries. The boundary conditions will be given by the analytical potential function

$$\phi = \sin\left(k_x x + k_y y\right)\exp\left(k_z z\right), \tag{23}$$

where $k_z = \sqrt{k_x^2 + k_y^2}$.

A Quadratic Boundary Element Method (QBEM), a Fast Multipole Accelerated QBEM (FMA-QBEM) and the present HPC method are used to solve the same problem. The cube is discretized by uniformly distributed

$Nx \cdot Ny \cdot Nz$ grid points, where *Nx*, *Ny* and *Nz* are number of grid point in the *x*-, *y*- and *z*-directions, respectively. See Fig.4 for an illustration of the discretization. The BEM-based methods use only the grid points on the boundaries with ϕ as unknown on Neumann surfaces and $\partial\phi/\partial n$ as unknown on the Dirichlet surface, while the unknowns in the HPC method are ϕ values on all the grid points.

As the QBEM and the FMA-QBEM are not the main interests of the present paper, we shall only summarize briefly some of their numerical aspects. The studied boundary element based methods solve the boundary integral equation

$$C(\mathbf{x})\phi(\mathbf{x}) = \iint_S \left[\frac{\partial \phi}{\partial n}(\mathbf{y}) G(\mathbf{x},\mathbf{y}) - \phi(\mathbf{y}) \frac{\partial G}{\partial n}(\mathbf{x},\mathbf{y}) \right] dS(\mathbf{y}) \quad , \tag{24}$$

which is the consequence of applying Green's 2nd identity to the Laplace equation. $\mathbf{x}$ and $\mathbf{y}$ are the location vectors of the field point and the singularity point, respectively. $C(\mathbf{x})$ is the solid angle coefficient. $\vec{n}$ is the normal vector on the surface, which is defined as positive pointing out of the fluid domain. $G(\mathbf{x},\mathbf{y}) = 1/|\mathbf{x}-\mathbf{y}|$ is a Rankine source. The adopted QBEM uses 8-node quadratic boundary elements to discrete the boundary surfaces enclosing the fluid domain. Thus the boundary geometry, the velocity potential and its normal derivatives are approximated by the quadratic shape functions. The resulting dense matrix is solved by GMRES with a diagonal preconditioner. The basis of the QBEM can be found in, for instance, Kim [21], Liu et al [28] and Teng et al. [49]. An important numerical issue of the higher-order BEM (HOBEM) is the evaluation of solid angle and Cauchy Principle Value (CPV) integrals in the boundary integral equations. In the present study, the solid angle is calculated based on a method by Montic [35]. The CPV integrals are obtained directly with the assistance of a triangle polar-coordinate transformation technique. See Li *et al.* [26] and Shao [45] for more details.

Because the conventional BEMs result in asymmetric dense matrices, the computational cost increases dramatically as the number of unknowns increases. Therefore, the fast multipole accelerated (FMA) method algorithm has been proposed to accelerate the efficiency and reduce the requirement on the computer memory. FMA was introduced by Rokhlin [43] as an O (*N*) numerical method for solving an integral equation for 2D Laplace equation. This method was further developed and made famous by Greengard [16] as he applied FMA to multi-body problems. FMA and related methods found applications in various fields in science and engineering. A comprehensive review of the history of the development of FMA can be found in, for instance Nishimura [37]. The applications of FMA in marine technology and costal engineering have been made by, for instance, Teng *et al.* [49], Fochesato and Dias [14] and Grilli et al. [17]. In this study, the above mentioned QBEM is also accelerated by a FMM code implemented by Shao [44], which is called FMA-QBEM in this article. One key point of the FMM is that the kernels $G(\mathbf{x},\mathbf{y})$ and $\frac{\partial G}{\partial n}(\mathbf{x},\mathbf{y})$ in Eq. (24) can be expanded into harmonic functions if the field point is well separated from a boundary element. For example

$$G(\mathbf{x},\mathbf{y}) = \frac{1}{r} = \sum_{n=0}^{p} \sum_{m=-n}^{n} \bar{S}_{n,m}(\mathbf{x}-\mathbf{y}_c) R_{n,m}(\mathbf{y}-\mathbf{y}_c), \quad |\mathbf{y}-\mathbf{y}_c| < |\mathbf{x}-\mathbf{y}_c| \ , \tag{25}$$

Here $\mathbf{y}_c$ is the expansion center close to singularity point $\mathbf{y}$ and the overbar indicates the complex conjugate. The functions $R_{n,m}$ and $S_{n,m}$ are called solid harmonic functions, which are complex and can be found in the

text book by Liu [27] and Shao [45]. p is the number of truncated terms used in the expansion. In the present FMA-QBEM, the resulting equations are solved by GMRES with block-diagonal preconditioner [36].

Fig.5 compares the accuracy of the present HPC method and the QBEM. The associated boundary conditions are specified by k_x=0.5 and k_y=1.0 in Eq.(23). The L_2 errors of the $\partial\phi/\partial n$ and ϕ on the Dirichlet surface and Neumann surface respectively are shown. The L_2 error for a function f is defined as

$$L_2\ error = \sqrt{\sum_{j=1}^{n}\left(f_{an}^{j}-f_{num}^{j}\right)^2 \Big/ \sum_{j=1}^{n}\left(f_{an}^{j}\right)^2} \tag{26}$$

Here f_{an}^{j} and f_{num}^{j} are the exact and numerical result at the j-th point, respectively. n is the total number of points involved in the evaluation of the L_2 errors. In the HPC method, the normal velocity on the Dirichlet surface is evaluated by Eq.(22). In order to make fair comparisons, the L_2 errors are plotted versus the elements size of the quadratic elements, e.g. $\Delta h = 2\Delta x = 2\Delta y = 2\Delta z$ in Fig.5. Δx, Δy and Δz are the mesh sizes along x-, y- and z-directions, respectively. The power curve fits of errors in Fig.5 as function of Δh gives

$$\left[L_2\ error\right]_D^{QBEM} \approx 7.968\cdot 10^{-3}\cdot\left(\Delta h\right)^{2.712},\quad \left[L_2\ error\right]_N^{QBEM} \approx 4.038\cdot 10^{-3}\cdot\left(\Delta h\right)^{3.610}, \tag{27}$$

$$\left[L_2\ error\right]_D^{HPC} \approx 1.371\cdot 10^{-2}\cdot\left(\Delta h\right)^{3.346},\quad \left[L_2\ error\right]_N^{HPC} \approx 4.014\cdot 10^{-3}\cdot\left(\Delta h\right)^{3.896}, \tag{28}$$

which indicate the rate of convergence of the solutions. The subscripts N and D mean the Neumann and Dirichlet surfaces, respectively. It is seen that the present HPC method has better performance than the QBEM in terms of accuracy on both the Dirichlet and Neumann surfaces. The HPC method has higher than k=3 convergence rate, which is expected as we have used all the 3rd order harmonic polynomials in constructing the harmonic polynomial cells. It is also expected that a QBEM using quadratic shape functions has approximately k=2 convergence rate, as it is confirmed in the analysis.

When satisfying the Neumann boundary condition in the present version of HPC method, we are using cells centered at the grid points in fluid (away from the Neumann surfaces).The latter fact has lowered the accuracy of our method. It was shown by Shao & Faltinsen [47] in a 2D HPC method that the accuracy by using harmonic polynomials interpolation are much higher close to the center of cell than that on the boundary points. It can be understandable if we make the analogy to the finite difference method, where the central difference has higher accuracy than forward/backward difference. It is therefore expected that the accuracy of the present HPC method can be further improved when ghost points are used outside the fluid domain. In the present work, we have not pursuit in this way and will leave it for future studies.

Fig.6 compares the CPU time used in the different methods. In order to make the comparison possible, the CPU time is plotted versus the number of unknowns in the boundary element based methods. For example, Nx=Ny=Nz=21 corresponds to 8448 unknowns in QBEM or FMA-QBEM and 79,507 unknowns in HPC. With the considered number of unknowns on boundaries, it is clearly demonstrated that the HPC method has better performance compared with QBEM and FMA-QBEM. The power curve fitting is also done in order to see how the computational time grows with the number of unknowns on the boundaries. As we discussed earlier, the conventional BEMs are O (N^2) methods. This is confirmed in Fig.6, where the CPU time of QBEM increases like the power of k=2.082. The computational time of FMA-QBEM grows like k=1.335 and k=1.241 for p=12 and p=15, respectively. The parameter p has been defined associated with Eq. (25), which is a

measure of the number of the spherical harmonics used in the expansion. The CPU time for the FMA-QBEM is higher for a larger p value. The grow rate for the present HPC method is k=1.782, which is higher than the FMA-QBEM.

The asymptotic behavior of CPU-time performance of a FMA-BEM and a volume method like the HPC method is case dependent. For the water wave modelling over a large horizontal area, the number of meshes along the vertical direction is very small compared with that in the horizontal directions. In this case, the CPU time of the volume method will scale linearly with increasing size of the problem and always be faster than a FMA-BEM. In a general case when the number of meshes increases along all directions, the asymptotic behavior of FMA-BEM will over-perform the volume method. However, when the number of unknowns on the boundary surfaces is of order of 10,000 (typical in marine hydrodynamics), the HPC method is preferred, considering both the accuracy and the efficiency.

Fig.7 shows the L_2 errors on both Dirichlet surface and Neumann surface as a function of Nx for Nz=10, 20 and 30, respectively. The associated boundary conditions are specified by the analytic solution in Eq. (23) with $k_x = k_y = 2\pi$. In general, for a fixed Nz value, the numerical errors decrease with increasing Nx. However, the decreasing rate slows down when Nx has reached a certain number. Further, increasing Nx does not significantly decrease the error. This means the resolution along the z-direction starts to govern the accuracy when Nx is sufficiently large.

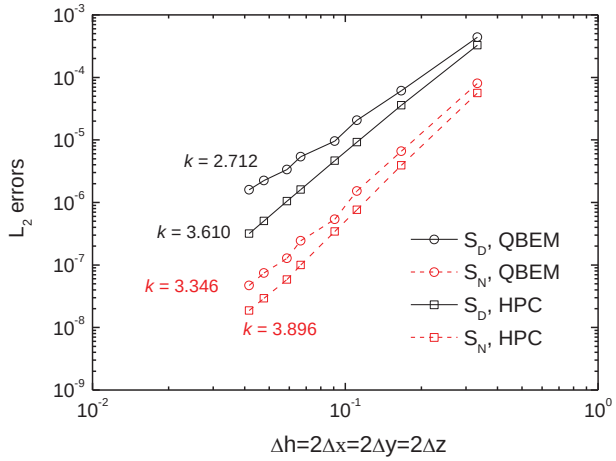

Fig.5. The L_2 errors on the Dirichlet surface (S_D) and Neumann Surfaces (S_N), respectively. The comparison is made based on a mixed Dirichlet-Neumann boundary value problem defined on a unit cube.

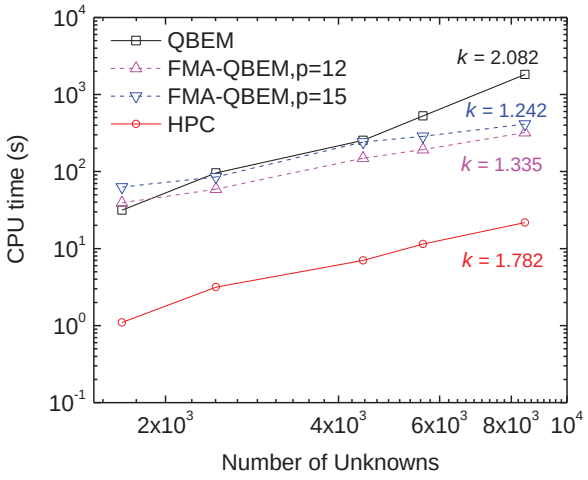

Fig.6. The comparison of CPU time versus number of unknowns on the boundary surfaces. Here the number of unknowns is that of QBEM based methods. The comparison is made based on a mixed Dirichlet-Neumann boundary value problem defined on a unit cube.

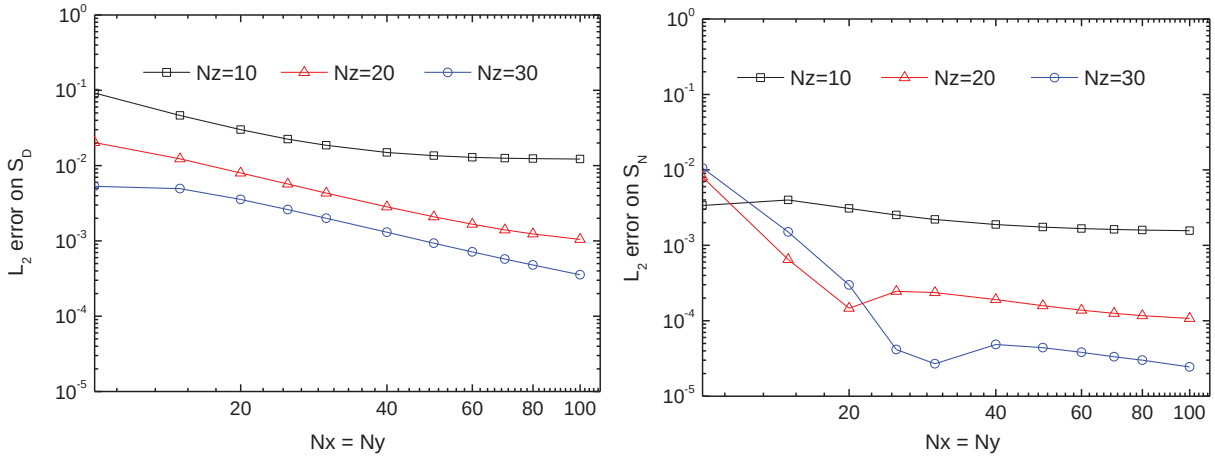

(a) (b)

Fig.7. L_2 errors as a function of number of grid points along x-direction for different mesh resolution along z-direction. The number of elements along y-direction is same as that on the x-direction. (a) On Dirichlet surface. (b) On Neumann surfaces. The study is made based on a mixed Dirichlet-Neumann boundary value problem defined on a unit cube.

4.2 A study on a shoe box

A mixed Dirichlet-Neumann boundary value problem on a rectangular shoe box is studied in this section. The velocity potential within the box is given by the analytical linear wave potential solution

$$\phi = \frac{\cosh k_z \left(z+h\right)}{\cosh k_z h} \sin\left(k_x x + k_y y\right) \tag{29}$$

where $k_z = \sqrt{k_x^2 + k_y^2} = 2\pi / \lambda$ with λ as the wave length. The domain has a length of $L = 8\lambda$, a width of $B = 2\lambda$ and depth of $D = 0.5\lambda$. The boundary-value problem is set with the top surface of the box as the Dirichlet boundary and the rest of the box surface as the Neumann boundary. The associated boundary conditions are specified by the analytic solution in Eq. (29) with k_y =0. The same case has been studied by Yan & Liu [55] by using the *p*-FFT accelerated QBEM. A similar case was also investigated by Sung and Grilli [48] by Fast Multipole Accelerated Cubic BEM (FMA-CBEM).

To be consistent with Yan & Liu [55] and Sung & Grilli [48], the numerical errors are defined as the absolute difference between the analytical and numerical solutions, normalized by dividing by the maximum value of the associated variable on the corresponding boundary. Errors are calculated for the normal velocity on the Dirichlet boundary S_D, and the potential on the Neumann surface S_N. The maximum errors ε^{m} and the average errors ε^a on both the Dirichlet surface and Neumann surfaces are presented in Fig.8. The power curve fits of error in Fig.8 as function of relative grid size gives

$$\varepsilon_D^a \approx 3.802\left(\Delta x/\lambda\right)^{3.983};\ \varepsilon_D^m \approx 85.267\left(\Delta x/\lambda\right)^{4.362} \tag{30}$$

$$\varepsilon_N^a \approx 2.750\left(\Delta x/\lambda\right)^{3.919};\ \varepsilon_N^m \approx 7.638\left(\Delta x/\lambda\right)^{3.736} \tag{31}$$

Higher than 3 convergence rates are achieved based on HPC method for the maximum and average errors on both the Dirichlet and Neumann surfaces. This is expected, because the present HPC method is 3rd order accurate as we have explained in Section 3. The convergence rates of ε^{m} and ε^a given by *p*-FFT accelerated QBEM [55] are respectively 2.47 and 2.29 on the Dirichlet surface, and they are respectively 3.30 and 3.49 on the Neumann surfaces. In Sung & Grilli [48], the predicted convergence rates of ε^{m} and ε^a by FMA-CBEM are respectively 3.57 and 3.48 on the Dirichlet surface, while the corresponding convergence rates of ε^{m} on Neumann surface is 4.04. As expected, the convergence rate of the HPC method is approximately one order faster than the *p*-FFT accelerated QBEM. Both the HPC and FMA-CBEM have higher than 3 convergence rate on both the Dirichlet and Neumann surfaces. On the other hand, the convergence rate of HPC is slightly higher than FMA-CBEM while it is slightly lower than FMA-CBEM on the Neumann surface.

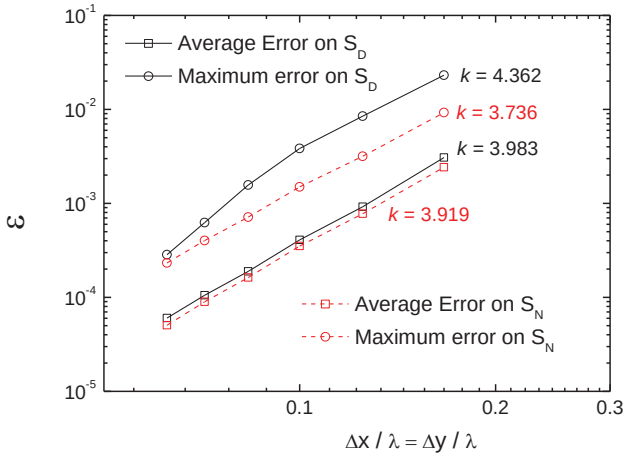

Fig.8. Numerical errors on the Dirichlet boundary and Neumann boundaries as function of normalized mesh size. Both the average errors and maximum errors are presented. The study is made based on a mixed Dirichlet-Neumann boundary value problem defined on a shoe box by using HPC method.

4.3 Comparison with a Finite Difference Method

It can be understood from Section 3 that the HPC method has similarities with the Finite Difference Method (FDM). The HPC method differs from an FDM solver in the choice of the interpolation basis and the exchange of a discrete Laplace equation in the body of the fluid with interpolation of the potential. Therefore, it is of interest to compare the accuracy of the present HPC method with a higher-order FDM.

To verify the convergence of higher-order 2D FDMs with possible application in modelling of travelling waves, Bingham and Zhang [1] considered a wave-type analytical solution similar to Eq.(29) on a periodic domain in the horizontal axis. The vertical velocity on the mean free surface is obtained numerically through FD solutions. The analysis confirmed that relative error decreases approximately with power 2, 4, and 6 for second-order, fourth-order and sixth-order FDMs when the mesh size in the horizontal axis is small enough. A similar study is made through the HPC solution to get the vertical velocity on free surface from the velocity potential. The relative errors for different Nz are shown in Fig.9. Nx=500 and Ny=500 have been used so that the mesh sizes in x- and y-directions have negligible influence on the accuracy. The presented HPC results are based on vertically uniform grids. The decay rate of the relative error with respect to Nz is 3.323 for the studied case. This agrees with the fact that the present HPC method is 3rd order accurate. It is also interesting to see that, the overall errors are actually lower than the fourth order FDM solution in [1] for the same Nz numbers using vertically uniform grid, even though the fourth order FDM has a better convergence rate which is approximately 4.0.

The number of stencil points in FDM is case dependent. An example is the water wave modelling. When the horizontal grid lines are parallel to the x- and y-axis of the Cartesian coordinate system and the σ-transformation is applied in the vertical direction, the fourth-order 3D FDM has 13 stencil points. See e.g. Engsig-Karup et al. [7]. For the bottom-mounted structures extending vertically throughout the depth of the fluid, 2D transformation in the horizontal plane may be applied so that the projections of grids in the horizontal plan are rectangular. An application can be found in Engsig-Karup and Bingham [6]. In this case, the stencil has 29 nodes for a fourth-order 3D FDM scheme. In a general case when none of the grid lines is in parallel with the grid axis, the 3D stencil has 125 nodes for the fourth-order FDM.

The designed HPC method in this article always uses 3D stencils of 27 points. The consequence is that if the same mesh is used in the fourth-order FDM and HPC method, the HPC method might be more expensive with the water-wave modelling and the bottom-mounted structure with constant sections, considering the actual number of the stencil nodes and the fact that the HPC method needs to solve interpolation coefficients through Eq.(15). In the numerical study of the wave focusing due to bottom topography which will be shown in Section 5.3, 30% to 40% of the total CPU time was spent on solving the equation system in Eq.(15). However, in order to make a fair comparison in terms of CPU time, one should consider the CPU efforts required to reach a given accuracy for each model, which is out of the scope of this article. For the water wave modelling in a finite constant-depth domain, an even more efficient method than FDM and the HPC method might be the high-order spectral (HOS) method, as discussed in e.g. Ducrozet et al. [4].

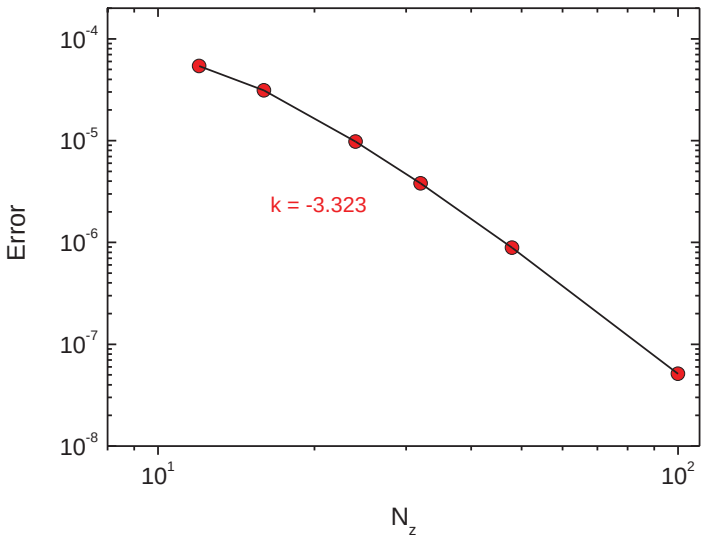

Fig.9. Convergence of the free-surface vertical velocity from free-surface velocity potential at *kh*=4. The Nx =Ny= 500 is used for the horizontal discretization. Uniform grid along vertical direction is used.

5. Time-domain wave-body simulations

In Section 5, we will study the fully-nonlinear wave making as well as wave-body interaction problems. A free-surface tracking method which only describes the water phase in order to accurately describe the dynamic and kinematic free-surface conditions is adopted. In order to describe the free surface in the fully-nonlinear studies, a generalized Mixed Eulerian-Lagrangian method similar as presented by Faltinsen [10] is used. The original Mixed Eulerian-Lagrangian method was first introduced by Ogilvie [38]. Considering the following time derivative

$$\frac{\delta}{\delta t} = \frac{\partial}{\partial t} + \vec{v} \cdot \nabla , \tag{32}$$

the fully nonlinear free-surface conditions are given as

$$\frac{\delta \phi}{\delta t} = -g\eta - \frac{1}{2}\nabla\phi \cdot \nabla\phi + \vec{v} \cdot \nabla\phi , \text{ on z=}\eta \tag{33}$$

$$\frac{\delta \eta}{\delta t} = \frac{\partial \phi}{\partial z} + \left(\vec{v} - \nabla\phi\right) \cdot \nabla\eta , \text{ on z=}\eta . \tag{34}$$

Here η is the wave elevation. When $\vec{v} = \nabla\phi$ is used, the free-surface particles are tracked in a Lagrangian manner, while $\vec{v} = \{0, 0, \delta\eta/\delta t\}$ leads to a semi-Lagrangian approach.

The spatial derivatives of the velocity potential are easily calculated by taking the derivatives of the harmonic polynomial in Eq. (19). The obtained velocities based on harmonic polynomials also satisfy Laplace equation. This property cannot be easily achieved if a finite-difference or a curve-fitting technique is used to calculate the spatial derivatives of the velocity potential. In order to obtain the spatial derivative of the wave elevation, a cubic-order polynomial fitting technique has been used.

In all the time-domain analysis presented in this paper, a 4th order explicit Runge-Kutta scheme is used to integrate the free-surface conditions in time in order to update the instantaneous free-surface position and the velocity potential on it. The instantaneous wetted body surface is also updated at each time instant. A free surface-fitted and body-fitted grid is used in the discretization of the fluid domain. An example of the grid system used for liquid sloshing in tank is shown in Fig. 10.

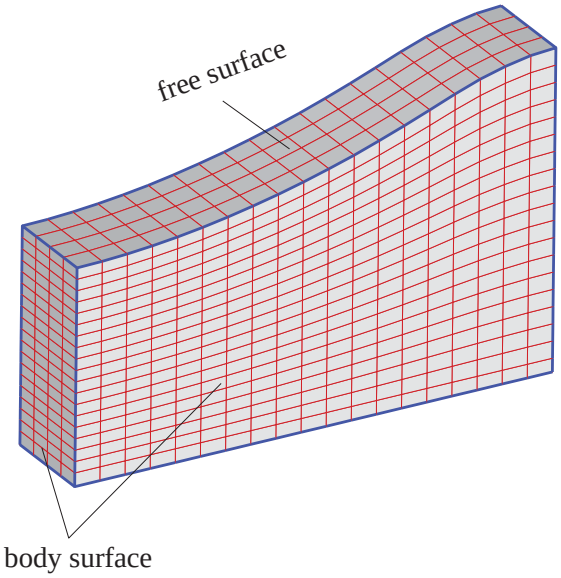

Fig. 10. Example of the body-fitted and free-surface fitted grid for a 3D sloshing tank.

A numerical damping zone is applied to act as a wave beach. The limitation of a fully-nonlinear potential-flow is that the numerical simulation will inevitably break down when the wave breaking is occurring. On the other hand, the aliasing errors accumulating at high frequencies eventually lead to undesirable instabilities. Presently, we are using the 5-point low-pass filter [30] every 5-30 time steps to prevent the so-called saw-tooth numerical instabilities [30] when some steeper waves are simulated. A better way of eliminating this instability is to convert the wave elevation and velocity potential on the free surface to a wavenumber space and cut off the wave components of the 1/3 highest wavenumbers.

5.1. Sloshing in a 3D rectangular tank

To investigate the validity of the present HPC method in the nonlinear wave-body interaction applications, the sloshing in 3D rectangular tanks is first simulated. The dimensions of the studied tank are chosen as L/h=2.0 and B/h=2.0 where L, B and h are the length, breadth and the water depth, respectively. The tank is forced to oscillate in surge with $x_T / h = 0.0186\sin\left(0.999\omega_1 t\right)$ along the tank length. Here ω_1 is the lowest natural frequency of the tank in surge. In the numerical simulations, the initial condition for wave elevation and velocity potential on the free surface are $\eta\left(x, y, t=0\right)=0$ and $\phi\left(x, y, z=\eta, t=0\right)=U_T\left(t=0\right)x$, respectively. Here U_T is the surge velocity of the tank, and x is the x-coordinate of a point on the free surface. This case has been experimentally studied by Okamoto & Kawahara [39] and numerically examined by Wu *et al.* [54] using a fully-nonlinear potential-flow Finite Element Method (FEM). Fig.11(a) and (b) present the wave profiles measured from the tank bottom along a tank at different time instants. The wave profiles at

$t\sqrt{g/h} = 13.0667$ and $t\sqrt{g/h} = 15.725$ agree very well with the experimental data [39] and Wu et al's [54] FEM results. The nonlinearity of the wave motion in the tank is clearly seen due to the fact that the wave crest is higher above the mean free surface than the distance between the mean free surface and the wave trough.

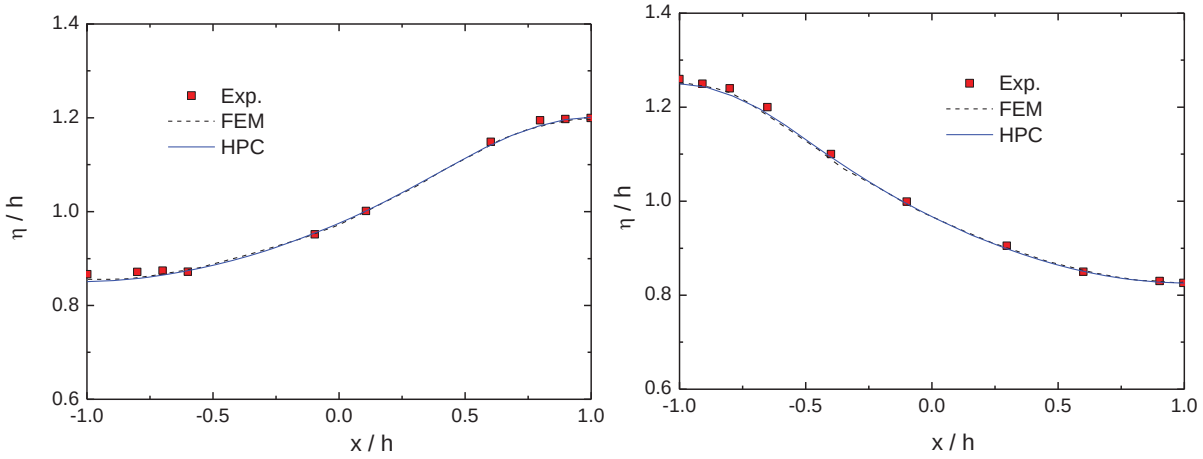

Fig.11. Wave profile along the tank at two time instants. Tank dimensions are defined by *L*/*h*=2.0 and *B*/*h*=2.0. The tank is forced to oscillate in surge with displacement $x_T / h = 0.0186\sin(0.999\omega_1 t)$. h is the mean water depth. ω_1 is the lowest natural frequency in surge. (a) $t\sqrt{g/h} = 13.0667$; (b) $t\sqrt{g/h} = 15.725$.

Fig.12(a) and Fig.12(b) show the time histories of wave elevation at the left tank walls for two other cases. The two cases are earlier studied by Frandsen [15] using fully-nonlinear time-domain inviscid FDM. The tank is forced to oscillate in *x*- and *z*-directions with prescribed displacements $x_T = A_h \cos(\omega_h t)$ and $z_T = A_v \cos(\omega_v t)$, respectively. Here z_T is the vertical displacement. ω_h and ω_v are the frequencies of the forced motions in *x*- and *z*-direction, respectively. The amplitudes of the forced oscillations are defined by the parameters $k_v = A_v\omega_v^2 / g$ and $k_h = A_h\omega_h^2 / g$. Here g is the gravity acceleration. An initial free surface elevation is also introduced as $\eta(x, y, t=0) = A_\varepsilon \cos(\pi x / L)$, where $\varepsilon = A_\varepsilon\omega_1^2 / g$ is used to define the initial wave profile nonlinearity. The initial condition for velocity potential on free surface is $\phi(x, y, z=\eta, t=0) = U_T(t=0)x + W_T(t=0)z$. Here U_T and W_T are the surge and heave velocities of the tank. In the 3D HPC method, we have used *L*/*h*=2.0 and *B*/*h*=2.0 in the simulations.

The results in Fig.12(a) correspond to k_v =0.5, k_h =0.0, ω_v =0.798 ω_1 and ε =0.0014, while k_v =0.5, k_h =0.0014, ω_v =0.798 ω_1, ω_h =0.98 ω_1 and ε =0.0 are used in Fig.12(b). As seen in Fig.12(b), the wave amplitude is building up with time. This building up of the wave elevation is due to the fact that the forcing frequency in surge is close to the lowest natural frequency in surge.

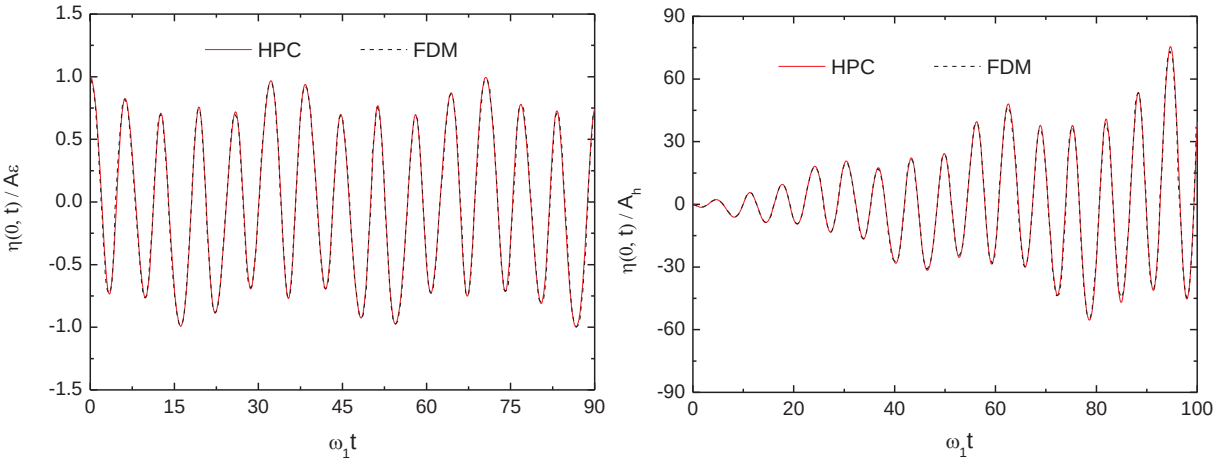

(a) (b)

Fig.12. Time history of wave elevation at the left tank wall due prescribed tank motion. (a) Forced vertical motion with initial free surface disturbance. k_v =0.5, k_h =0.0, ω_v =0.798 ω_1 and ε =0.0014; (b) Combined forced horizontal and vertical motions without initial free surface disturbance. k_v =0.5, k_h =0.0014, ω_v =0.798 ω_1 , ω_h =0.98 ω_1 and ε =0.0.

The flow motions studied in Fig.11 and Fig.12 are all in two dimensions. The transient waves in a sloshing tank with 3D effects are also simulated by the HPC method. The tank is a square-based tank with *L*=*B*=1*m*. The mean water depth is *h*=0.25*m*. The tank is forced to oscillate only horizontally with at an excitation angle of 30^o. The displacement of the oscillation is given as a sine function x_T =0.005$L\sin(\omega t)$, which means the excitation amplitude of the tank along the *x* and *y* axes are $0.005L\ \sin(\omega t)\cos(30^o)$ and $0.005L\sin(\omega t)\sin(30^o)$, respectively. The wave elevation is recorded at a probe located on the diagonal of the square base with 6.36*cm* away from the left-lower corner of the tank.

The comparison between the present numerical results and the experimental results of Wu *et al.* [52] is shown in Fig.13. The results in Fig.13(a) and Fig.13(b) correspond to excitation frequencies $\omega = 0.90\omega_1$ and $\omega = 0.93\omega_1$, respectively. In general, the comparisons show good agreements. The HPC method is able to predict the beating phenomenon in the transient phase of the fluid motion, especially in the first a few oscillations where damping effects is negligible. In the experimental result shown in Fig.13(b), the amplitudes of the wave modulation decay slightly due to physical damping effects in the tank, while the HPC method does not show any decay. There are many sources of damping in a sloshing tank. Examples are those due to breaking waves, interior structures and boundary layer on the tank walls. See, for instance, the text book by Faltinsen & Timokha [12]. For the clean tank studied here without interior structures and local breaking waves, it is believed that the boundary layer effect is the dominant damping source. In order to introduce rational damping mechanism in the potential-flow calculations, a proper boundary layer theory may be used to estimate the damping due to the boundary layers. Faltinsen & Timokha [12] have discussed how to combine the linear boundary layer theory with potential-flow theory for the linearized steady-state sloshing problems. The idea was later applied to the moonpool problem by Kristiansen [24]. The effect of the boundary layer is an out/in flow to the potential flow domain. In the fully-nonlinear potential-flow studies, one may combine the nonlinear boundary layer theory with the fully-nonlinear potential flow formulation outside the boundary layer.

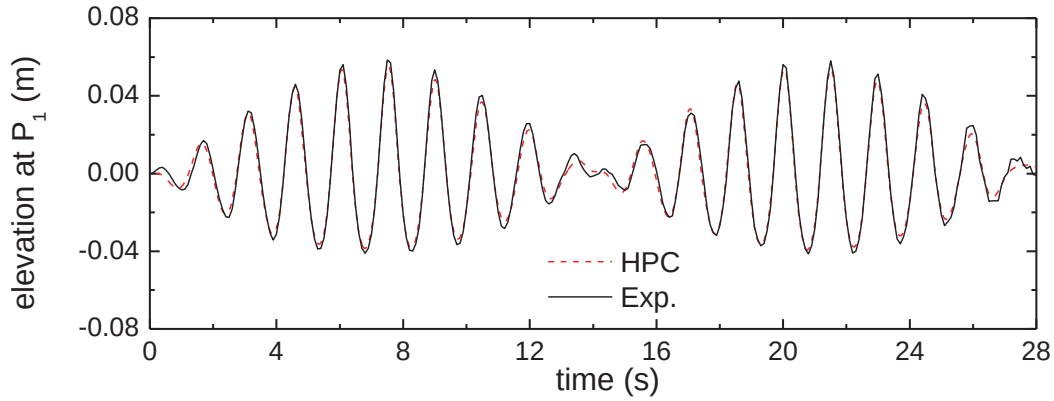

(a)

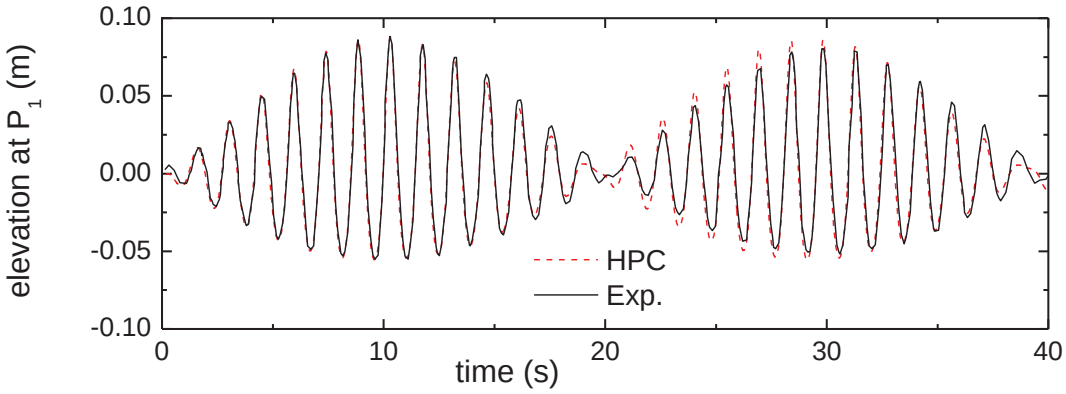

(b)

Fig.13. Time history of wave elevation at a probe close to the left-lower corner of a 3D tank under forced surge and sway oscillations. The present numerical results are compared with the experimental results of Wu et al. [52]. The forced displacement in *x*- and *y*-directions are $x_T = 0.005L\cos(30^0)\sin(\omega t)$ and $y_T = 0.005L\sin(30^0)\sin(\omega t)$, respectively. ω is the excitation frequency. *L*=*B*=1.0*m*, *h*=0.25*m*. (a) $\omega = 0.90\omega_1$ (b) $\omega = 0.93\omega_1$.

5.2. Shallow water wave tank with flat bottom

Regular waves generated in a wave tank with horizontal bottom are simulated. A piston wave maker is located at the left end of the tank while a numerical wave beach is applied on the other end. The position of the intersection point between the free surface and the piston wave maker is obtained by using $\vec{v} = (U_{wm}, \phi_y)$ in Eq.(34). Here U_{wm} is the horizontal velocity of the piston wave maker. The semi-Lagrangian approach is adopted elsewhere on the free surface. A body-fitted and free surface-fitted structured mesh, which is updated each time step, is used in the fully-nonlinear analysis. See section 5.1.

The first four harmonics are obtained by Fourier analysis of the wave elevations along the tank. The numerical results will be compared with the experiments by Chapalain et al. [2]. The experimental characteristics and the wave parameters of the studied case are listed in Table 1. Here *h* is the water depth. *e* is half of the stroke of the piston wave maker. *T* is the linear wave period. The wave parameters α and β are defined as $\alpha=A/h$ and $\beta = h/\lambda$, respectively. *A* and λ are wave amplitude and wave length, respectively. $Ur=\alpha/\beta^2$ is the Ursell number. Fig.14 shows the wave amplitudes of different harmonics along the wave tank for '*Trial A*' of Chapalain *et al.*

[2] with generally good agreement. There are some notable discrepancies in the second-order wave amplitude between the numerical results and the experiment, which may be partly due to the viscous effects in the shallow water tank. By adding a very small Rayleigh damping in the dynamic free surface condition, Shao & Faltinsen [46] have shown in the same shallow water numerical wave tank by using the 2D HPC method that the damping effects on the higher-order harmonics are non-negligible. The amount of the damping used was only 25% of that suggested by Chapalain *et al.* [2] according to the experiments.

Table 1. The experimental characteristics and wave parameters

Trial	*h (m)*	*e (m)*	*T (s)*	α	β	U_r
A	0.4	0.078	2.5	0.105	0.084	14.9

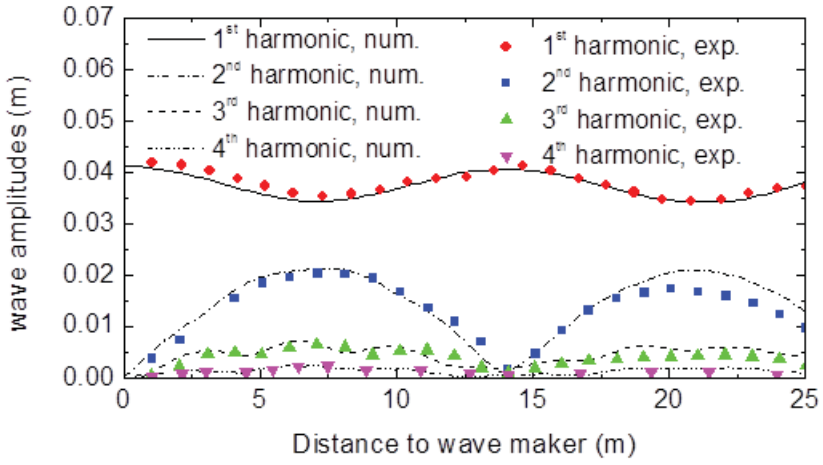

Fig.14. The wave amplitudes for different harmonics of the wave elevation along the tank. The wave parameters are given in Table 1.

5.3. Wave focusing due to bottom topography

Whalin [51] conducted laboratory experiments concerning wave focusing over a bottom topography that acts as a focusing lens. The wave tank used in the experiments has the horizontal dimensions $25.603m \times 6.096m$. The waves were generated by a piston wave maker and propagate from $0.4572m$ water depth to a shallower region with $0.1524m$. In the middle portion of the wave tank, $7.62m$ < x <$15.24m$, semicircular steps were evenly spaced leading to shallower portion of the channel. A sketch of the tank bottom and calm water surface is illustrated in Fig.15, which has been exaggerated 15 times in the vertical direction.

In the numerical model, the still water depth is defined as follows:

$$h(x,y)=\begin{cases}0.4572, & -20.0 \le x \le 10.67 - G(y)\\ 0.4572 + \dfrac{1}{25}(10.67 - G(y) - x), & 10.67 - G(y) < x < 18.29 - G(y)\\ 0.1524, & 18.29 - G(y) \le x \le 35.0\end{cases} \tag{35}$$

where $G(y) = \sqrt{y(6.096 - y)}$. A piston wave maker is equipped at the left end (deeper region) to generate the target waves, with its stroke estimated by a linear wave-maker theory [3]. A damping zone is applied near the shallower end in order to absorb right-going waves. The presence of the bottom topography generates a left-going diffraction wave, which may later be reflected by the wave maker and propagate into the focusing region we are interested in. It is not clear how much reflection effects from the wave maker exist in the measured data from the model tests. So it was decided to stop the numerical simulation before the reflected waves from the wave makers have arrived the focusing region. In order to have sufficient time window for the harmonic analysis of the wave elevations at different locations, we have used a 20*m* longer deeper-region close to the wave maker than in the experiments. See the definition of still water depth in Eq.(35). The arrival time of the above mentioned reflected wave to the focusing region is first estimated based on the group velocity of a linear wave, and the numerical simulation is then terminated before that time. In this way, the numerical results are not influenced by the reflected waves from the wave maker. However, some differences between the numerical and experimental results are expected, which are assumed as small.

The following two cases with different wave heights are studied in this paper: (1) T=2.0s, A=0.0075m, kA=0.012; (2) T=2.0s, A=0.0106m, kA=0.017. Here T, A, k are wave period, linear wave amplitude and wave number, respectively. Fig.16 and Fig.17 show the comparion of the present numerical results with the experiments results for the two cases, respectively. The first-, second-, and third-harmonic wave amplitudes are all in good agreement, especially in the focusing region where the nonlinear effects matter. A bird-eye view of the contour plot of the velocity potential on the free surface at the end of the simulation is presented in Fig.18. In this figure, the same color indicates the same level of the value of velocity potential. The waves show a 2D behavior closer to the wave maker and build up 3D effects when propagating over the bottom topography.

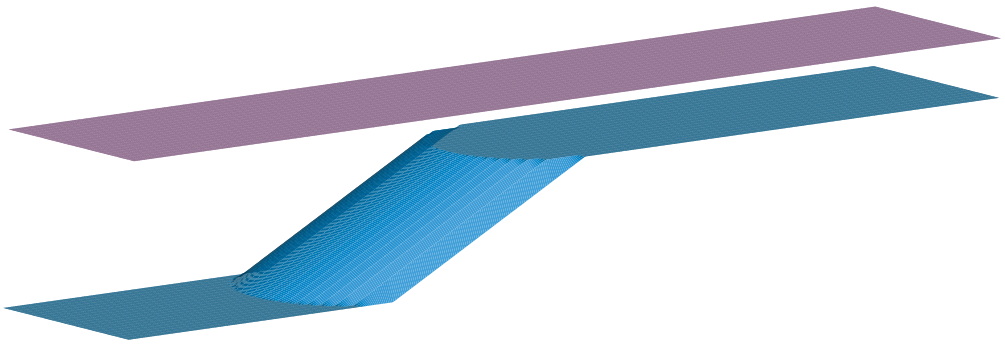

Fig.15. Sketch of the tank bottom and calm water surface (exaggerated 15 times in vertical direction).

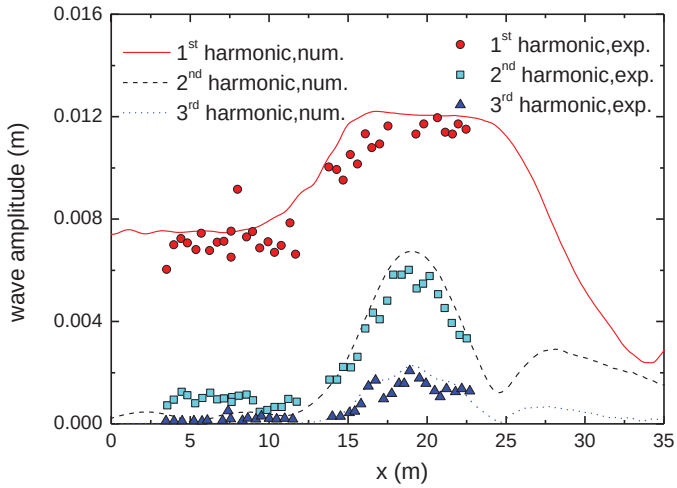

Fig.16. The wave amplitues of the first, second and third harmonics. Wave period T=2.0s. Half of wave height A=0.0075m. kA=0.012. k is the wave number. The numerical results based on the present HPC method are compared with the Whalin [51]'s exeperimental results.

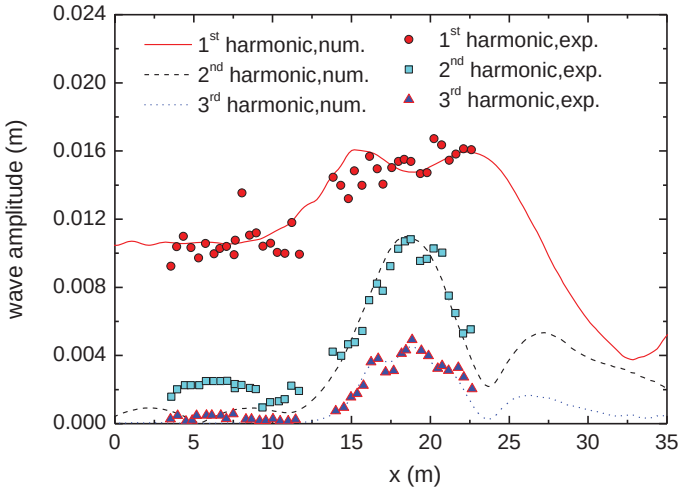

Fig.17. The wave amplitues of the first, second and third harmonics. Wave period T=2.0s. Half of wave height A=0.0106m. kA=0.017. k is the wave number. The numerical results based on the present HPC method are compared with the Whalin[51]'s exeperimental results.

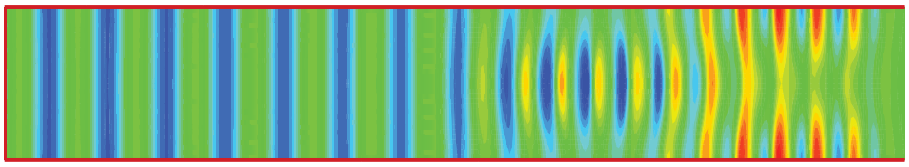

Fig.18. The contour plot of velocity potential on the free surface at the end of the simulation. The same color indicates the same level of the value of velocity potential. The left end is close to wave maker, while the damping zone is on the right end.

5.4. Nonlinear wave diffraction on a bottom-mounted vertical circular cylinder

A bottom-mounted free-surface piercing vertical circular cylinder in nonlinear regular waves is studied. An explicit part of the solution representing the incident waves is separated from the total solution and only the rest part of the solution is considered as unknown. This separation of an explicit solution has also been used by Ferrant [13] in his fully-nonlinear potential-flow boundary element method. Recently, Ducrozet et al. [5] has carefully analyzed the performance of this separation technique using several 2D linear and nonlinear test cases. In the present numerical analysis, the explicit part of the solution is modeled by a stream function method [42]. The advantage of separating an explicit solution is that we can use fine mesh close to the body and coarse mesh away from the body, because the 3D scattered waves by the structure decay with the distance to the body. An example of the discretization of the fluid domain near the bottom-mounted vertical cylinder is shown in Fig.19. The ratio between the outer cylinder diameter and body cylinder diameter is about 23.

In this study, we consider a deep water cases with kR=0.245. Here k is the wave number and R is the radius of the cylinder. The same cases have been studied experimentally by Huseby & Grue [18] and numerically by Ferrant [13] using a fully-nonlinear potential-flow boundary element method. The adopted boundary element method was based on linear triangular boundary elements. In the time-domain simulation of the present HPC method, the time history of the horizontal force on the cylinder is first recorded and Fourier analysis is performed when steady state has been achieved. Fig.20-Fig.23 show the results for first, second, third and fourth harmonics, respectively. Both the amplitudes and phases of the harmonics are presented for different wave steepness. The phase angle is defined relative to the incident wave elevation at the vertical axis of the cylinder. t=0 is the time when the crest of the incident wave comes to the vertical axis of the cylinder and phases are defined relative to this time. In the figures, A is the incident wave amplitude defined as half of the wave height. The present numerical results are compared with the experimental results of Huseby & Grue [18], fully-nonlinear numerical results of Ferrant [13] and the analytical results of Malenica & Molin [34] based on 3rd order perturbation method. The perturbation method assumes that the wave elevation is a small parameter compared with the diameter of the cylinder and the wave lengths.

In general, the present results are in good agreement with the numerical results of Ferrant [13], which are based on the same theoretical formulation as the present study. Furthermore, both the present numerical results and Ferrant's results are consistent with the perturbation method for small kA numbers. A clear discrepancy between the numerical results and the experimental results of the 2nd harmonic forces is seen. The reason is not known to us. Special care was taken in the experiments so that the second-order free waves (parasitic waves) have very small effects on the results. Since the second-order parasitic waves travel at half the speed of the main waves, they arrive at the cylinder at twice the time compared to when the leading part of the wave train arrives. A time window was chosen in the experiments after the leading part of the wave train has reached the cylinder, while the parasitic wave has not. The viscous forces on the cylinder were also estimated by a linear laminar boundary layer assumption, which were shown to be very small. The range of studied Keulegan-Carpenter numbers implies flow separation is possible. However, it is stated by Huseby and Grue[18] that flow separation was not visually observed.

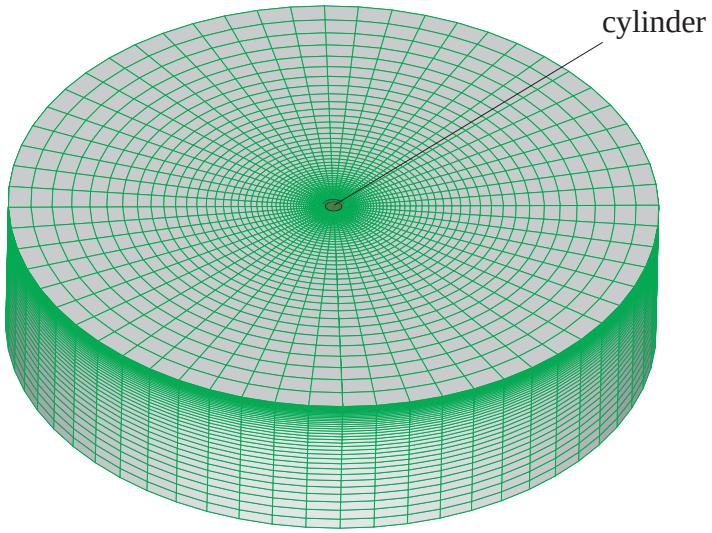

Fig.19. Discretization of the truncated fluid domain close to the bottom-mounted vertical circular cylinder. The ratio between the outer cylinder diameter and body cylinder diameter is approximately 23.

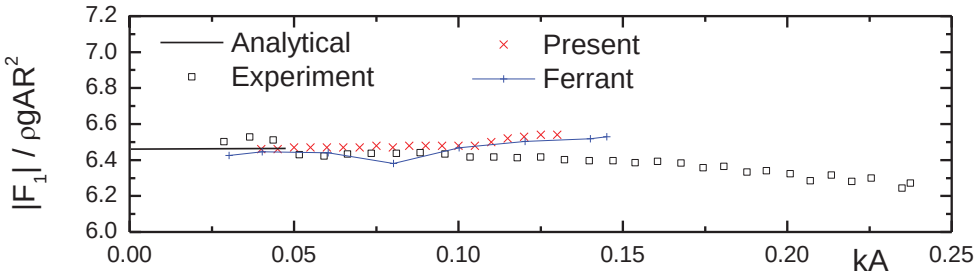

(a)

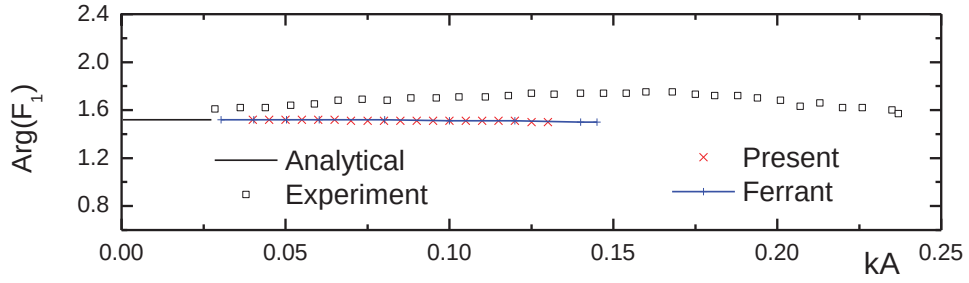

(b)

Fig.20. Comparison of the first-harmonic horizontal force on the bottom-mounted vertical cylinder in regular waves. *kR*=0.245. R is the radius of the cylinder. *k* is the wave number. A is half the wave height. Deep water condition is considered. (a) Force amplitudes. (b) Phases of the forces.

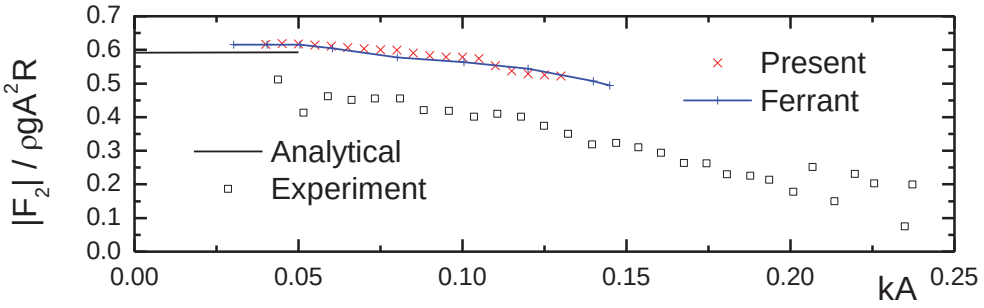

(a)

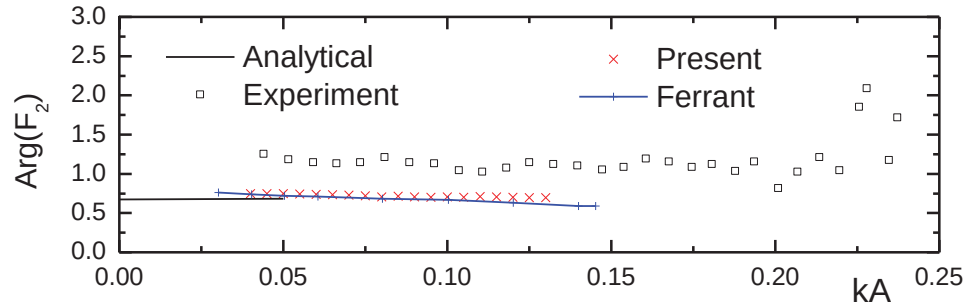

(b)

Fig.21. Comparison of the second-harmonic horizontal force on the bottom-mounted vertical cylinder in regular waves. *kR*=0.245. R is the radius of the cylinder. *k* is the wave number. A is half the wave height. Deep water condition is considered. (a) Force amplitudes. (b) Phases of the forces.

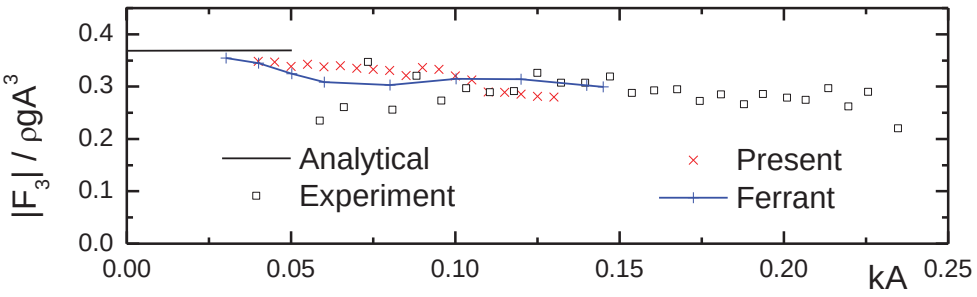

(a)

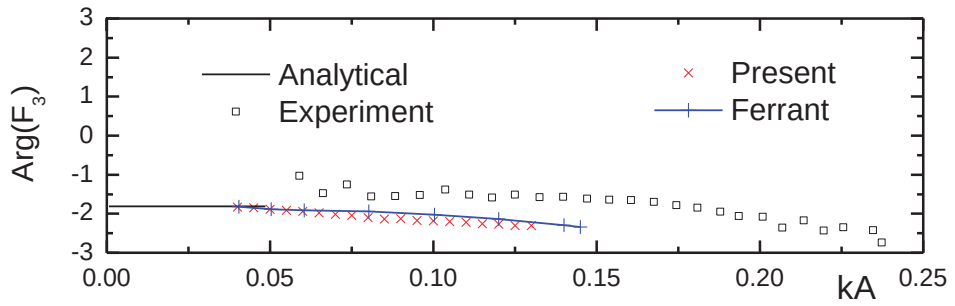

(b)

Fig.22. Comparison of the third-harmonic horizontal force on the bottom-mounted vertical cylinder in regular waves. *kR*=0.245. R is the radius of the cylinder. *k* is the wave number. A is half the wave height. Deep water condition is considered. (a) Force amplitudes. (b) Phases of the forces.

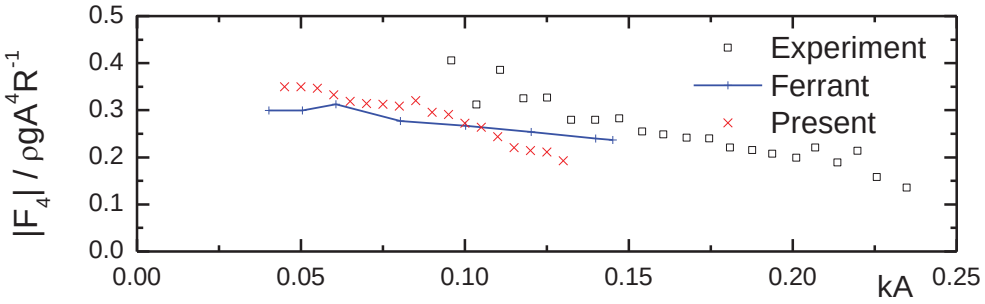

(a)

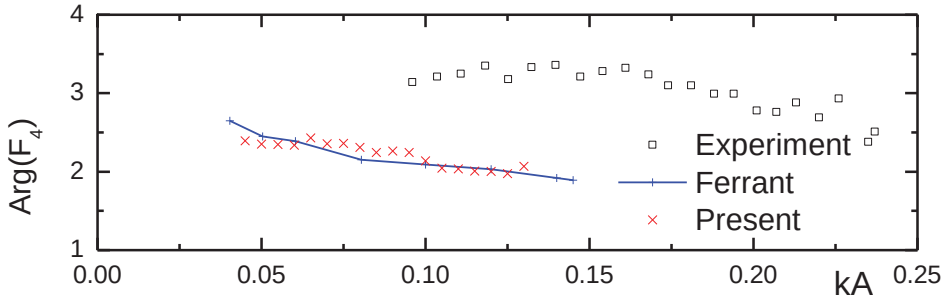

(b)

Fig.23. Comparison of the fourth-harmonic horizontal force on the bottom-mounted vertical cylinder in regular waves. *kR*=0.245. R is the radius of the cylinder. *k* is the wave number. A is half the wave height. Deep water condition is considered. (a) Force amplitudes. (b) Phases of the forces.

6. Conclusions and future studies

We have developed an efficient and accurate numerical method named as Harmonic Polynomial Cell (HPC) method to solve 3D Laplace equation. The computational domain is discretized by overlapping cells. Within each cell, the velocity potential is represented by the linear superposition of a set of complete harmonic polynomials, which are the elementary solutions of the 3D Laplace equation. The method is compared with Quadratic Boundary Element Method (QBEM) and Fast Multipole Accelerated QBEM (FMA-QBEM) by considering an idealized mixed Dirichlet-Neumann boundary value problem (BVP) on a cube. A BVP on a shoe box previously studied in the literature by pre-corrected fast Fourier transform (*p*-FFT) and Fast Multipole Accelerated Cubic BEM (FMA-CBEM) is also revisited. A Dirichlet-to-Neumann problem is also studied in order to compare with the 4th order FDM by Bingham and Zhang [1]. The convergence rate of the HPC method was shown to be between 3 and 4, while the accuracy was higher than the 4th order FDM for the considered problem using the same vertical meshes as [1]. Sufficiently fine horizontal meshes were used so that accuracy of the solution depends only on the vertical meshes. It is concluded that the present HPC method is a promising approach in terms of both accuracy and efficiency. Some fully-nonlinear time-domain applications of the HPC method in marine hydrodynamics are also presented, including the liquid sloshing in

3D tanks, shallow-water wave tank, nonlinear waves over bottom topography and nonlinear wave diffraction around a bottom-mounted vertical circular cylinder.

Since the presented HPC method utilizes harmonic polynomials as basis functions, problems with the convergence of the solutions at a sharp corner with flow singularity are expected. Local potential-flow solutions with singularities in derivatives must then be included. This deserves a separate study. Furthermore, the applications presented in this paper are limited to zero forward speed. In the future, the investigation will be made on applying the HPC method to study ships travelling in waves and offshores structures in combined waves and currents. To achieve that, efficient mesh generator shall be developed to handle complex marine structures. The most challenging part of the fully-nonlinear wave-body interaction analysis is how to properly handle the local wave breaking and post wave breaking, which will need dedicated future study.

Acknowledgement

We gratefully acknowledge the discussions of Prof. A.N. Timokha on harmonic polynomials. We also would like to thank Dr. C.H. Wu for sharing with us the experimental data of sloshing in the square-based tank.This work was supported by the Research Council of Norway through the Centres of Excellence funding scheme AMOS, project number 223254. The financial support from DNV GL when the first author is revising the paper is also appreciated.

Appendix

The 26 harmonic polynomials f_j (j=1,…,26) used in constructing the present harmonic polynomial cells are given as follows

$$f_1 = 1;\ f_2 = x;\ f_3 = y;\ f_4 = z;\ f_5 = x^2 - \tfrac{1}{2}(y^2 + z^2);\ f_6 = xy;\ g_7 = xz;\ f_8 = y^2 - z^2;\ g_9 = 2yz;$$

$$f_{10} = x^3 - \tfrac{3}{2}x\left(y^2 + z^2\right);\ f_{11} = x^2 y - \tfrac{1}{4}y(y^2 + z^2);\ f_{12} = x^2 z - \tfrac{1}{4}z(y^2 + z^2);\ f_{13} = x(y^2 - z^2);$$

$$f_{14} = 2xyz;\ f_{15} = y(y^2 - 3z^2);\ f_{16} = z(3y^2 - z^2);$$

$$f_{17} = x^4 - 3x^2\left(y^2 + z^2\right) + 3/8\left(y^2 + z^2\right)^2;\ f_{18} = x^3 y - \frac{3}{4}xy\left(y^2 + z^2\right);\ f_{19} = x^3 z - \frac{3}{4}xz\left(y^2 + z^2\right);$$

$$f_{20} = x^2\left(y^2 - z^2\right) - \frac{1}{6}\left(y^4 - z^4\right);\ f_{21} = 2x^2 yz - \frac{1}{3}yz\left(y^2 + z^2\right);\ f_{22} = y^4 - 6y^2 z^2 + z^4;$$

$$f_{23} = x^5 - 5x^3\left(y^2 + z^2\right) + \frac{15}{8}x\left(y^2 + z^2\right)^2;\ f_{24} = x^4 y - \frac{3}{2}x^2 y\left(y^2 + z^2\right) + \frac{1}{8}y\left(y^2 + z^2\right)^2;$$

$$f_{25} = x^4 z - \frac{3}{2}x^2 z\left(y^2 + z^2\right) + \frac{1}{8}z\left(y^2 + z^2\right)^2;$$

$$f_{26} = x^6 - \frac{5}{16}\left(y^6 + z^6\right) - \frac{15}{2}x^4\left(y^2 + z^2\right) + \frac{45}{8}x^2\left(y^2 + z^2\right)^2 - \frac{15}{16}y^2 z^2\left(y^2 + z^2\right).$$

References

[1] H.B. Bingham, H. Zhang, On the accuracy of finite difference solutions for nonlinear water waves. J. Eng. Math. 58 (2007) 211-228.

[2] G. Chapalain, R. Cointe, A. Temperville, Observed and modeled resonantly interacting progressive water-waves. Coastal Eng. 16 (1992) 267-300.
[3] R.G. Dean, R.A. Dalrymple, Water wave mechanics for engineers & scientists, World Scientific Publishing Company, 1991.
[4] G. Ducrozet, H.B. Bingham, A.P. Engsig-Karup, F. Bonnefoy, P. Ferrant : A Comparative Study of Two Fast Nonlinear Free Surface Water Wave Models, Int. Journal for Numerical Methods in Fluids 69 (11), 1818-1834, 2012.
[5] S. Ducrozet, A.P. Engsig-Karup, H.B. Bingham, P. Ferrant, A non-linear wave decomposition model for efficient wave–structure interaction. Part A: Formulation, validations and analysis, J. Comput. Phys. 257 (2014), Part A, 863-883.
[6] A.P. Engsig-Karup, H.B. Bingham, Boundary-fitted solutions for 3D nonlinear water wave-structure interaction. 24th International Workshop on Water Waves and Floating Bodies, Zelenogosk, Russia, 19-22 April, 2009.
[7] A.P. Engsig-Karup, H.B. Bingham, O. Lindberg, An efficient flexible-order model for 3D nonlinear water waves. J. Comput. Phys. 228 (2009) 2100-2118.
[8] A. P. Engsig-Karup, M. G. Madsen, S. L.Glimberg, A massively parallel GPU-accelerated model for analysis of fully nonlinear free surface waves. Int. J. Numer. Meth. Fluids 70 (2012) 20-36.
[9] L. Euler, Principles of the motion of fluids, Physica D: Nonlinear Phenomena 237 (2008) 1840-1854.
[10] O.M.Faltinsen, Numerical solution of transient nonlinear free-surface motion outside or inside moving bodies. in Wehausen, J. and N.Salvesen (Eds.), in Proc. 2nd Conf. on Num. Ship Hydrodynamics, U.C.Berkeley: University Extension Publications, 1977, pp. 347–357.
[11] O.M. Faltinsen, A.N. Timokha, Analytically approximate natural sloshing modes and frequencies in two-dimensional tanks, European Journal of Mechanics-B/Fluids, http://dx.doi.org/10.1016/j.euromechflu.2014.01.005.
[12] O.M. Faltinsen, A.N. Timokha, Sloshing, Cambridge University Press, 2009.
[13] P. Ferrant, Fully nonlinear interactions of long-crested wave packets with a three dimensional body. In Proceedings of 22nd ONR Symp. in Naval Hydrodynamics, 59-72, 1998.
[14] C. Fochesato, F. Dias . A fast method for nonlinear three-dimensional free-surface waves. Proc. R. Soc. Lond. A, Math. Phys. Eng. Sci. 465 (2006), 2715-35.
[15] J. B. Frandsen, Sloshing motions in excited tanks, J. Comput. Phys. 196 (2004) 53–87.
[16] L.F. Greengard, Rapid evaluation of potential fields in particle systems. PhD thesis, Yale Univ., New Haven, CT. Dept. of Computer Science, 1988.
[17] S.T. Grilli, F.Dias, P. Guyenne, C. Fochesato, F. Enet, Progress in fully nonlinear potential flow modeling of 3D extreme ocean waves. Chapter 3 in Advances in Numerical Simulation of Nonlinear Water Waves (Vol. 11 in Series in Advances in Coastal and Ocean Engineering). World Scientific Publishing Co. Pte. Ltd., 2010, 75-128.
[18] M. Huseby, J. Grue. An experimental investigation of higher harmonic wave forces on a vertical cylinder. J. Fluid Mech. 414 (2000) 75-103.
[19] A.B. Kennedy, J.D. Fenton, A fully-nonlinear 3-D method for the computation of wave propagation. in Proc. 25th Int. Conf. Coastal Eng., Orlando, 1, pp. 1102-1115.
[20] A.B. Kennedy, J.D. Fenton, A fully-nonlinear computational method for wave propagation over topography. Costal Engineering 32 (1997) 137-161.
[21] C.H. Kim. Nonlinear waves and offshore structures, Word Scientific Publishing Co. Pte. Ltd, 2008.
[22] F.T. Korsmeyer, Dick K.P. Yue, K. Nabors, J.K. White, Multipole-accelerated preconditioned iterative methods for three-dimensional potential problems, in: Proc Int Conf Boundary Elem Methods, Worcester, MA, 1993, pp. 517-527.

[23] F.T. Korsmeyer, T. Klemas, J. White, J. Phillips, Fast hydrodynamic analysis of large offshore structures. in: Proc. of the 9th Proc. Int. Offshore Polar Eng. Conf. (ISOPE), Brest, 1999. pp. 27-34.
[24] Kristiansen, T., Two-dimensional numerical and experimental studies of piston-mode resonance. PhD thesis, Dept of Marine Technology, NTNU, Trondheim, Norway, 2009.
[25] Laplace equation. (2004, June 27). In *Wikipedia, The Free Encyclopedia*. Retrieved 12:24, August 22, 2012, from http://en.wikipedia.org/w/index.php?title=Laplace_equation&oldid=16566818
[26] H.B. Li, G.M. Han, H.A. Mang. A new method for evaluating singular integrals in stress analysis of solids by the direct boundary element method. Int. J. Numer. Methods Eng. 21 (1985), 2071-2098.
[27] Y.J. Liu, Fast multipole boundary element method - theory and applications in engineering, Cambridge University Press, Cambridge, 2009.
[28] Y.H. Liu, C.H. Kim, S.X. Lu, Comparison of higher-order boundary element and constant panel method for hydrodynamic loadings, J. Offshore Mech. Arct. Eng. 1 (1991) 8-17.
[29] Y.J. Liu, N. Nishimura,The fast multipole boundary element method for potential problems: a tutorial, Eng. Anal. Bound. Elem. 30 (2006) 371-381.
[30] M.S. Longuet-Higgins, E.D.Cokelet, (1976). The deformation of steep surface waves on water: I. a numerical method of computation, Proc. R. Soc. Lond. A, Math. Phys. Sci. 350 (1976) 1-26.
[31] I.A., Lukovsky, M.Y. Barnyak, and A.N. Komarenko, Approximate Methods of Solving the Problems of the Dynamics of a Limited Liquid Volume. Kiev, Naukova Dumka (in Russian), 1984.
[32] Q.W.Ma, G.X.Wu, R. Eatock Taylor, Finite element simulation of fully non-linear interaction between vertical cylinders and steep waves. Part 1: Methodology and numerical procedure. Int. J. Numer. Meth. Fluids 36 (2001) 265–285.
[33] Q.W.Ma, G.X.Wu, R. Eatock Taylor, Finite element simulations of fully non-linear interaction between vertical cylinders and steep waves. Part 2: Numerical results and validation. Int. J. Numer. Meth. Fluids 36 (2001) 287-308.
[34] S. Malenica, B.Molin, Third-harmonic wave diffraction by a vertical cylinder. J. Fluid Mech. 302 (1995), 203-229.
[35] Montic, V., A new formula for the C-matrix in the Somigliana identity, J. Elast. 33 (1993), 191–201.
[36] T. Nishida, K. Hayami, Application of the fast multipole method to the 3D BEM analysis of electron guns. in: M. Marchettia, C.A. Brebbia, M.H. Aliabadi (Eds.), Boundary Elements XIX, Computational Mechanics Publications ,1997, pp.613-22.
[37] N. Nishimura, Fast multipole accelerated boundary integral equation methods. Appl. Mech. Rev. 55 (2002), 299-324.
[38] T.F. Ogilvie, Nonlinear high-Froude-number free-surface problems, J. Eng. Math. 1 (1967) 215-235.
[39] T. Okamoto and M. Kawahara, Two-dimensional sloshing analysis by Lagrangian finite element method, Int. J. Numer. Methods Fluids 11 (1990) 453-477.
[40] I. N. Vekua, On completeness of a system of harmonic polynomials in space. Doklady Akad. Nauk SSSR (NS) 90, 495–498, 1953.
[41] I. N. Vekua, New Methods for Solving Elliptic Equations. Wiley. 1967.
[42] M. M. Rienecker and J. D. Fenton. A Fourier approximation method for steady water waves. J. Fluid Mech. 104 (1981) 119-137.
[43] V. Rokhlin, Rapid solution of integral equations of classical potential theory. J. Comput. Phys. 60 (1985) 187-207.
[44] Y. Saad, M.H. Schultz, GMRES: A generalized minimal residual algorithm for solving nonsymmetric linear systems, SIAM J. Sci. Stat. Comput. 7 (1986) 856-869.
[45] Y.L. Shao. Numerical potential-flow studies on weakly-nonlinear wave-body interactions with/without small forward speeds. PhD thesis, Dept of Marine Technology, NTNU, Trondheim, Norway, 2010.

[46] Y.L. Shao, O.M. Faltinsen, Towards efficient fully-nonlinear potential-flow solvers in marine hydrodynamics. in: Proc. of the 31st Int. Conf. on Ocean, Offshore and Arc. Eng. (OMAE). Rio de Janeiro, Brazil, 2012.
[47] Y.L. Shao, O.M. Faltinsen, Numerical modeling of nonlinear water waves by a Harmonic Polynomial Cell (HPC) method with immersed free surface. Proceedings of the 31st International Conference on Ocean, Offshore and Arctic Engineering (OMAE2013). To appear.
[48] H.G. Sung, S.T. Grilli, BEM computations of 3-d fully nonlinear free-surface flows caused by advancing surface disturbances. Int. J. Offshore Polar Eng.18 (2008) 292-301.
[49] B. Teng, Y.Gou, D.Z. Ning. Higher order BEM for wave-current action on structures direct computation of free-term coefficient and CPV integrals China Ocean Eng. 20 (2006), 395-410.
[50] B. Teng, D.Z. Ning, Y. Gou, A fast multipole boundary element method for three-dimensional potential flow problems. Acta Oceanol. Sin. 23 (2004), 747-756.
[51] R.W. Whalin, The limit of applicability of linear wave refraction theory in a convergence zone, Research Report H-71-3, U.S. Army Corps of Engineers, WES, Vicksburg, MI, 1971.
[52] C.H.Wu, O.M. Faltinsen, B.F. Chen, Time-independent finite difference and ghost cell method to study sloshing liquid in 2d and 3d tanks with internal structures. Commun. Comput. Phys. 13 (2013) 780-800.
[53] G.X. Wu, R. Eatock Taylor, Time stepping solutions of the two-dimensional nonlinear wave radiation problem. Ocean Eng. 22 (1995) 785-798.
[54] G. X. Wu, Q. W. Ma, and R. Eatock Taylor, Numerical simulation of sloshing waves in a 3D tank based on a finite element method Appl. Ocean Res. 20 (1998) 337–355.
[55] H.Yan, Y. Liu, An efficient high-order boundary element method for nonlinear wave-wave and wave-body interactions. J. Comput. Phys. 230 (2011) 402-424.
[56] O.I.Yuldashev, M.B.Yuldasheva. 3D finite elements with harmonic basis functions for approximations of high order. JINR, Ell-2008-104, Dubna, 2008. Availale at: http://www1.jinr.ru/Preprints/2008/104(E11-2008-104).pdf.

Figure Captions
Click here to download Figure: figure captions.doc

Fig.1. A set of points where the velocity potentials are known.

Fig.2. Definition of the local index for a cell centered at grid point (i, j, k) indicated as point 27 in the figure.

Fig.3. An example of a harmonic polynomial cell containing 8 hexahedrons elements.

Fig.4. Discretization of a cube with top surface as a Dirichlet surface and the rest as Neumann surfaces.

Fig.5. The L_2 errors on the Dirichlet surface (S_D) and Neumann Surfaces (S_N), respectively. The comparison is made based on a mixed Dirichlet-Neumann boundary value problem defined on a unit cube.

Fig.6. The comparison of CPU time versus number of unknowns on the boundary surfaces. Here the number of unknowns is that of QBEM based methods. The comparison is made based on a mixed Dirichlet-Neumann boundary value problem defined on a unit cube.

Fig.7. L_2 errors as a function of number of grid points along x-direction for different mesh resolution along z-direction. The number of elements along y-direction is same as that on the x-direction. (a) On Dirichlet surface. (b) On Neumann surfaces. The study is made based on a mixed Dirichlet-Neumann boundary value problem defined on a unit cube.

Fig.8. Numerical errors on the Dirichlet boundary and Neumann boundaries as function of normalized mesh size. Both the average errors and maximum errors are presented. The study is made based on a mixed Dirichlet-Neumann boundary value problem defined on a shoe box by using HPC method.

Fig.9. Convergence of the free-surface vertical velocity from free-surface velocity potential at kh=4. Nx =Ny= 500 is used for the horizontal discretization. Uniform grid along vertical direction is used.

Fig. 10. Example of the body-fitted and free-surface fitted grid for a 3D sloshing tank.

Fig.11. Wave profile along the tank at two time instants. Tank dimensions are defined by L/h=2.0 and B/h=2.0. The tank is forced to oscillate in surge with displacement $x_T / h = 0.0186\sin\left(0.999\omega_1 t\right)$. h is

the mean water depth. ω_1 is the lowest natural frequency in surge. (a) $t\sqrt{g/h} = 13.0667$; (b) $t\sqrt{g/h} = 15.725$.

Fig.12. Time history of wave elevation at the left tank wall due prescribed tank motion. (a) Forced vertical motion with initial free surface disturbance. k_v =0.5, k_h =0.0, ω_v =0.798 ω_1 and ε =0.0014; (b) Combined forced horizontal and vertical motions without initial free surface disturbance. k_v =0.5, k_h =0.0014, ω_v =0.798 ω_1 , ω_h =0.98 ω_1 and ε =0.0.

Fig.13. Time history of wave elevation at a probe close to the left-lower corner of a 3D tank under forced surge and sway oscillations. The present numerical results are compared with the experimental results of Wu et al. [48]. The forced displacement in *x*- and *y*-directions are $x_T = 0.005L\cos(30^0)\sin(\omega t)$ and $y_T = 0.005L\sin(30^0)\sin(\omega t)$, respectively. ω is the excitation frequency. *L*=*B*=1.0*m*, *h*=0.25*m*. (a) $\omega = 0.90\omega_1$ (b) $\omega = 0.93\omega_1$.

Fig.14. The wave amplitudes for different harmonics of the wave elevation along the tank. The wave parameters are given in Table 1.

Fig.15. Sketch of the tank bottom and calm water surface (exaggerated 15 times in vertical direction).

Fig.16. The wave amplitues of the first, second and third harmonics. Wave period *T*=2.0s. Half of wave height *A*=0.0075m. *kA*=0.012. *k* is the wave number. The numerical results based on the present HPC method are compared with the Whalin[50]'s exeperimental results.

Fig.17. The wave amplitues of the first, second and third harmonics. Wave period *T*=2.0s. Half of wave height *A*=0.0106m. *kA*=0.017. *k* is the wave number. The numerical results based on the present HPC method are compared with the Whalin[50]'s exeperimental results.

Fig.18. The contour plot of velocity potential on the free surface at the end of the simulation. The same color indicates the same level of the value of velocity potential. The left end is close to wave maker, while the damping zone is on the right end.

Fig19. Discretization of the truncated fluid domain close to the bottom-mounted vertical circular cylinder. The ratio between the outer cylinder diameter and body cylinder diameter is approximately 23.

Fig.20. Comparison of the first-harmonic horizontal force on the bottom-mounted vertical cylinder in regular waves. kR=0.245. R is the radius of the cylinder. k is the wave number. A is half the wave height. Deep water condition is considered. (a) Force amplitudes. (b) Phases of the forces.

Fig.21. Comparison of the second-harmonic horizontal force on the bottom-mounted vertical cylinder in regular waves. kR=0.245. R is the radius of the cylinder. k is the wave number. A is half the wave height. Deep water condition is considered. (a) Force amplitudes. (b) Phases of the forces.

Fig.22. Comparison of the third-harmonic horizontal force on the bottom-mounted vertical cylinder in regular waves. kR=0.245. R is the radius of the cylinder. k is the wave number. A is half the wave height. Deep water condition is considered. (a) Force amplitudes. (b) Phases of the forces.

Fig.23. Comparison of the fourth-harmonic horizontal force on the bottom-mounted vertical cylinder in regular waves. kR=0.245. R is the radius of the cylinder. k is the wave number. A is half the wave height. Deep water condition is considered. (a) Force amplitudes. (b) Phases of the forces.

Figure 1

Click here to download Figure: fig.1.doc

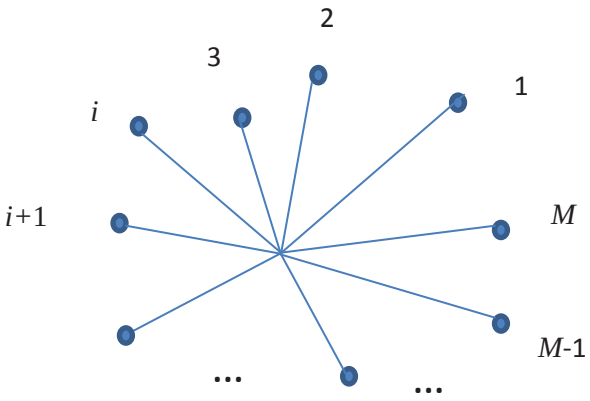

Figure 2

Click here to download high resolution image

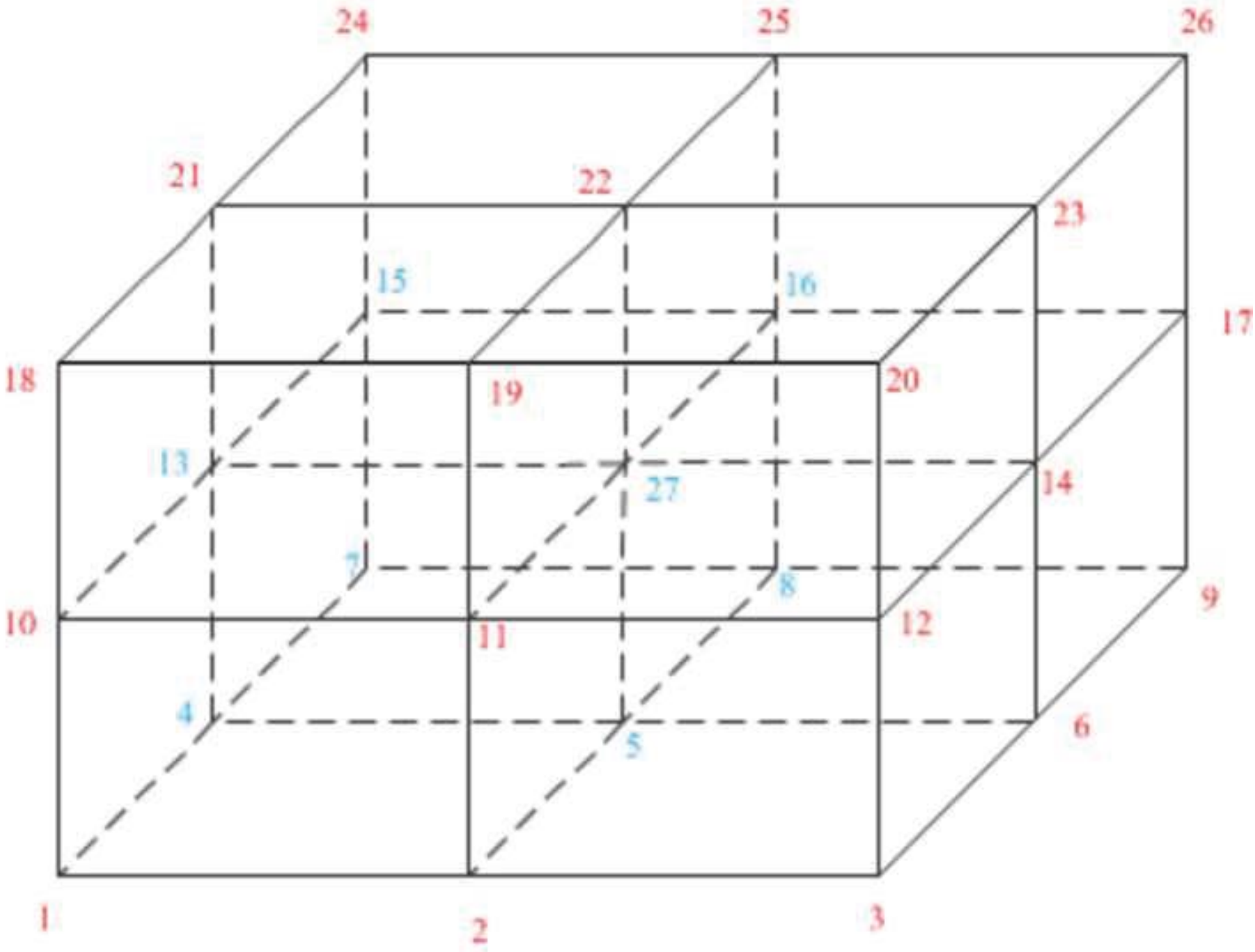

Figure 3

Click here to download high resolution image

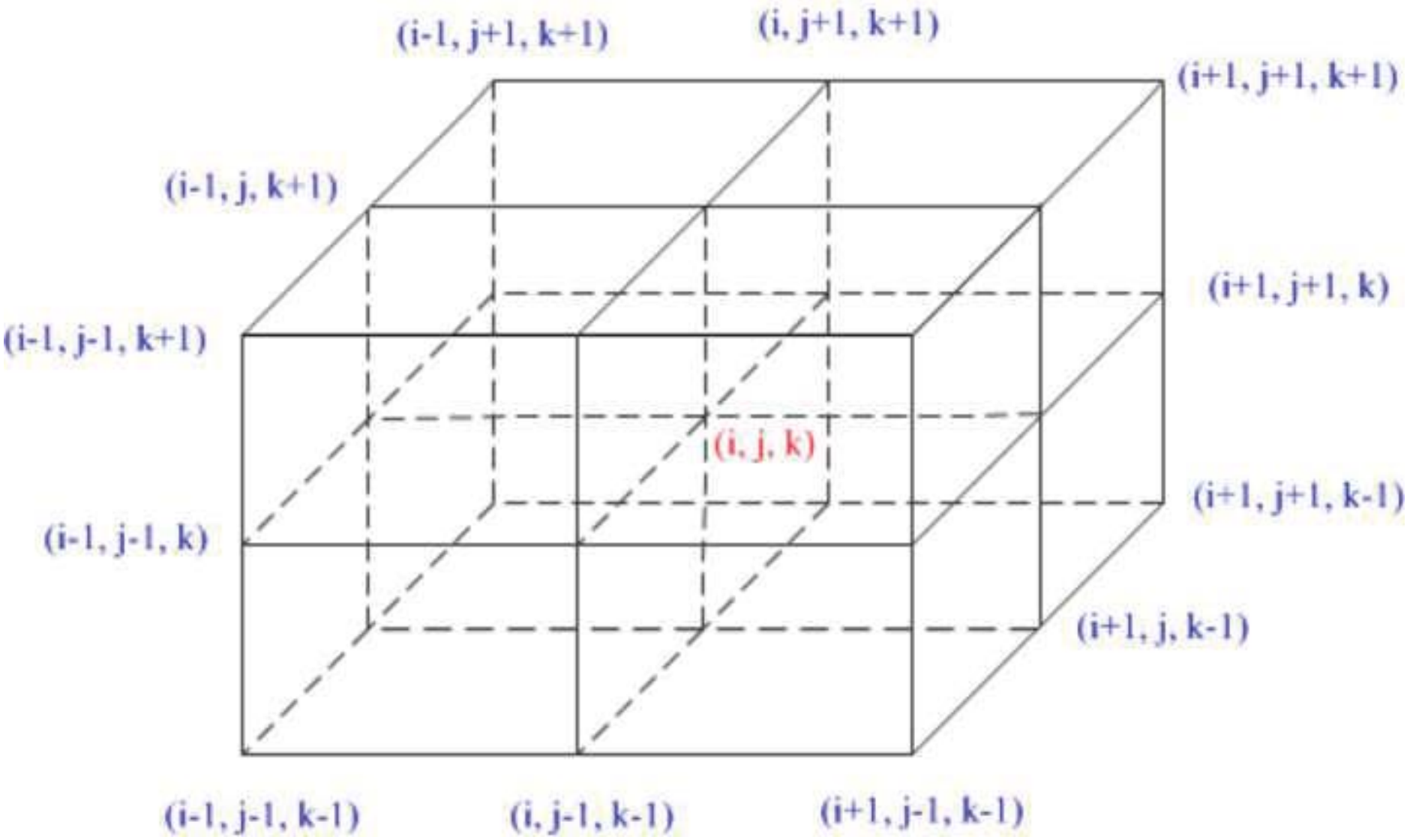

Figure 4

Click here to download high resolution image

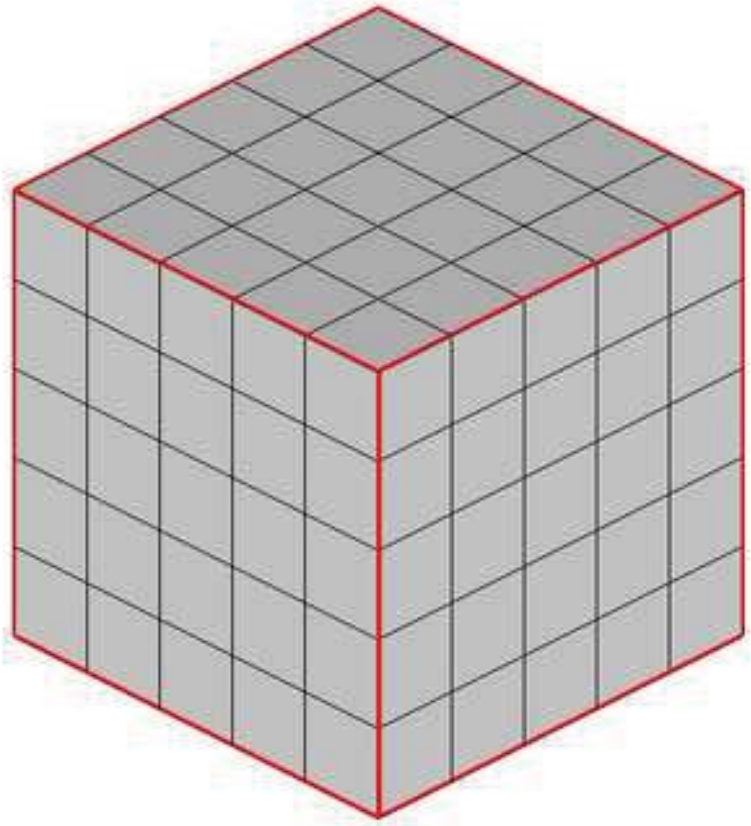

Figure 5
Click here to download high resolution image

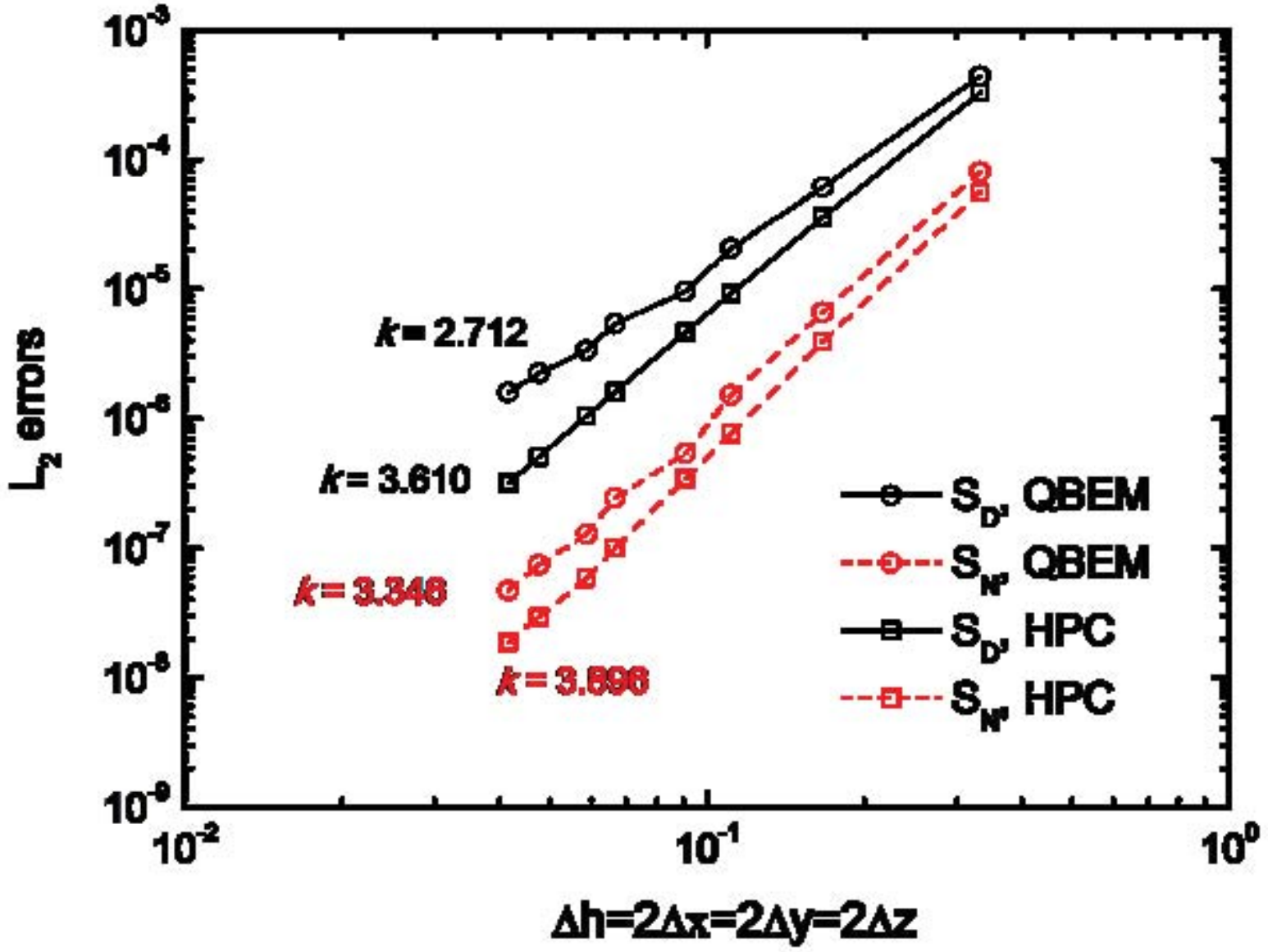

Figure 6
Click here to download high resolution image

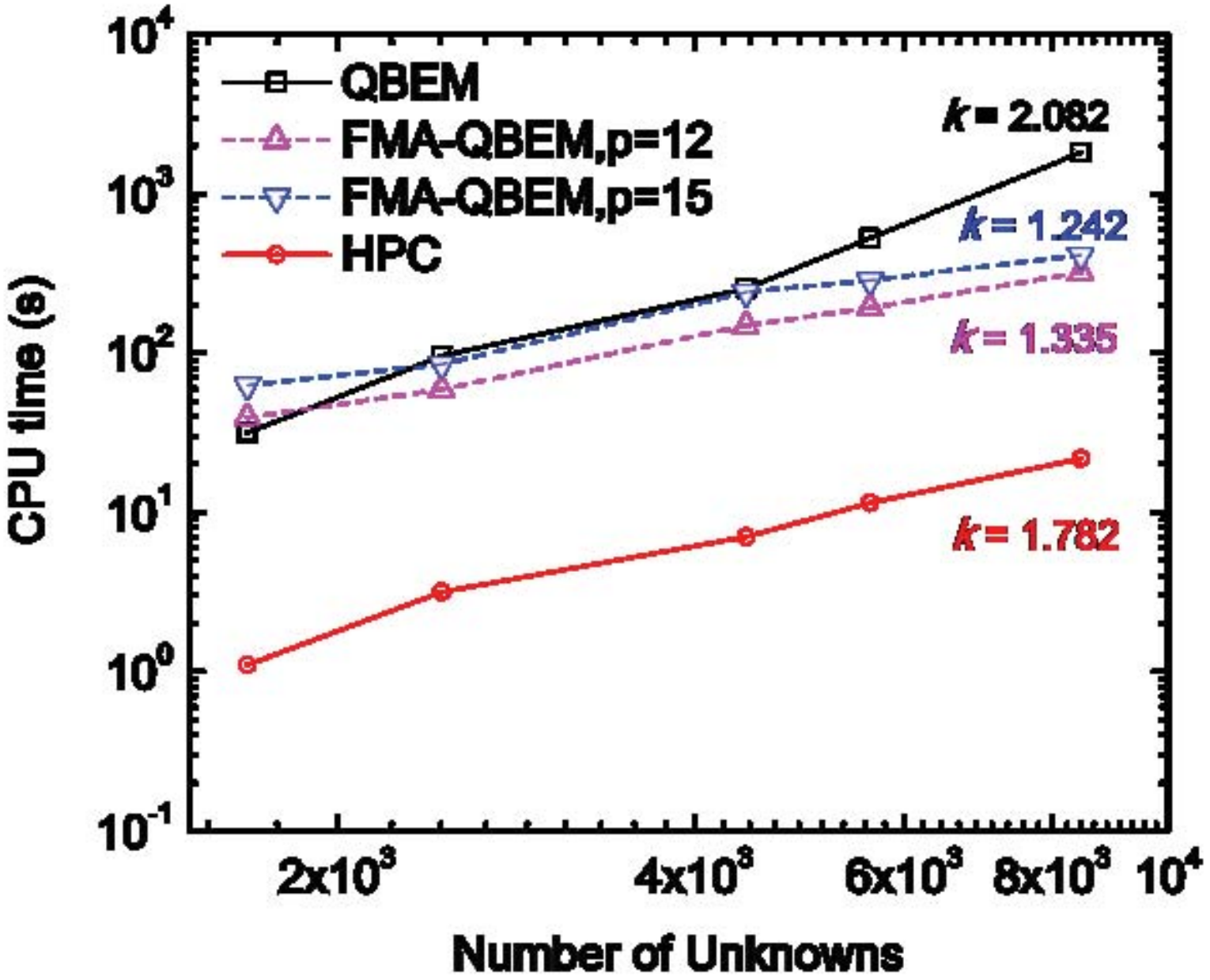

Figure 7a
Click here to download high resolution image

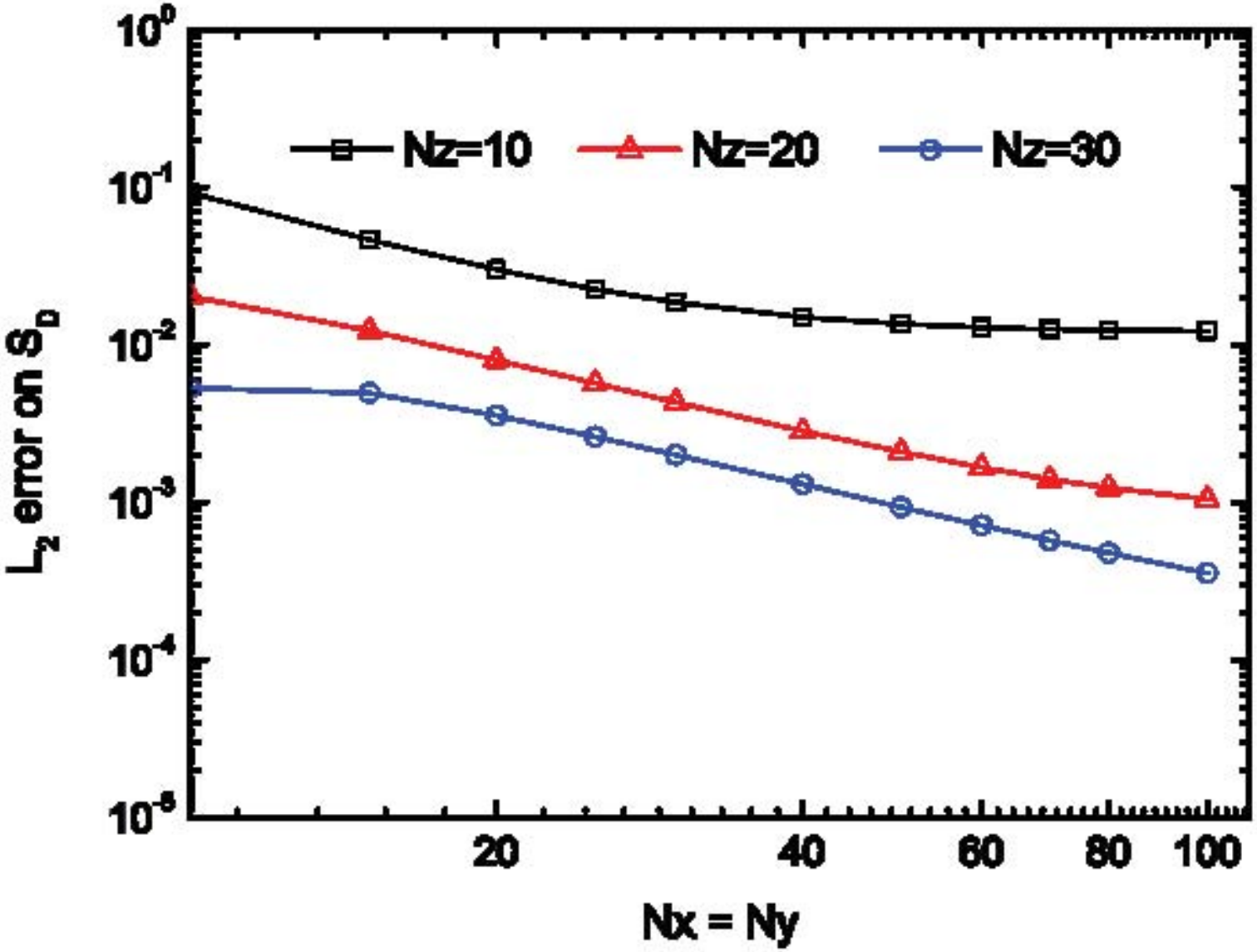

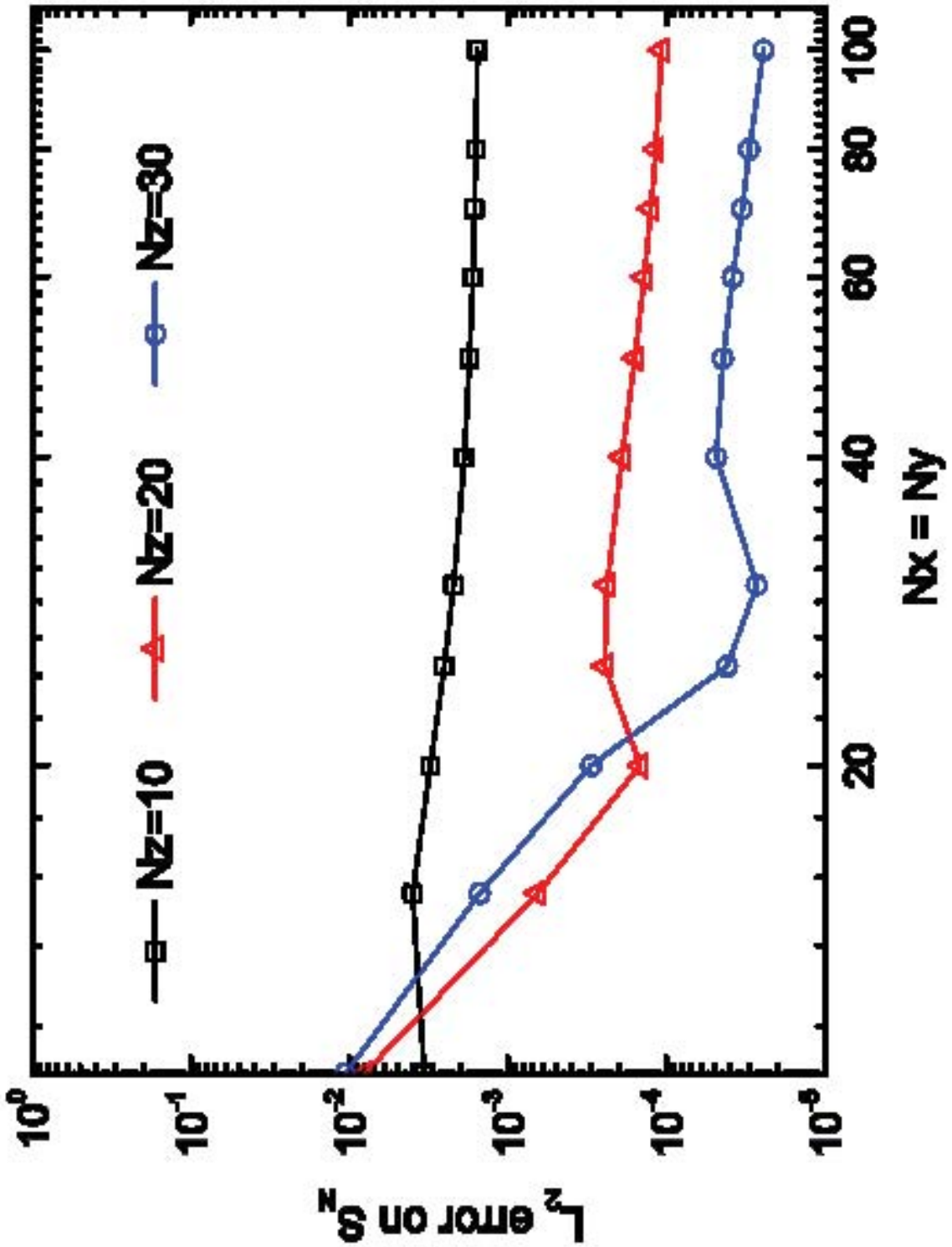

Figure 7b
Click here to download high resolution image

Figure 8
Click here to download high resolution image

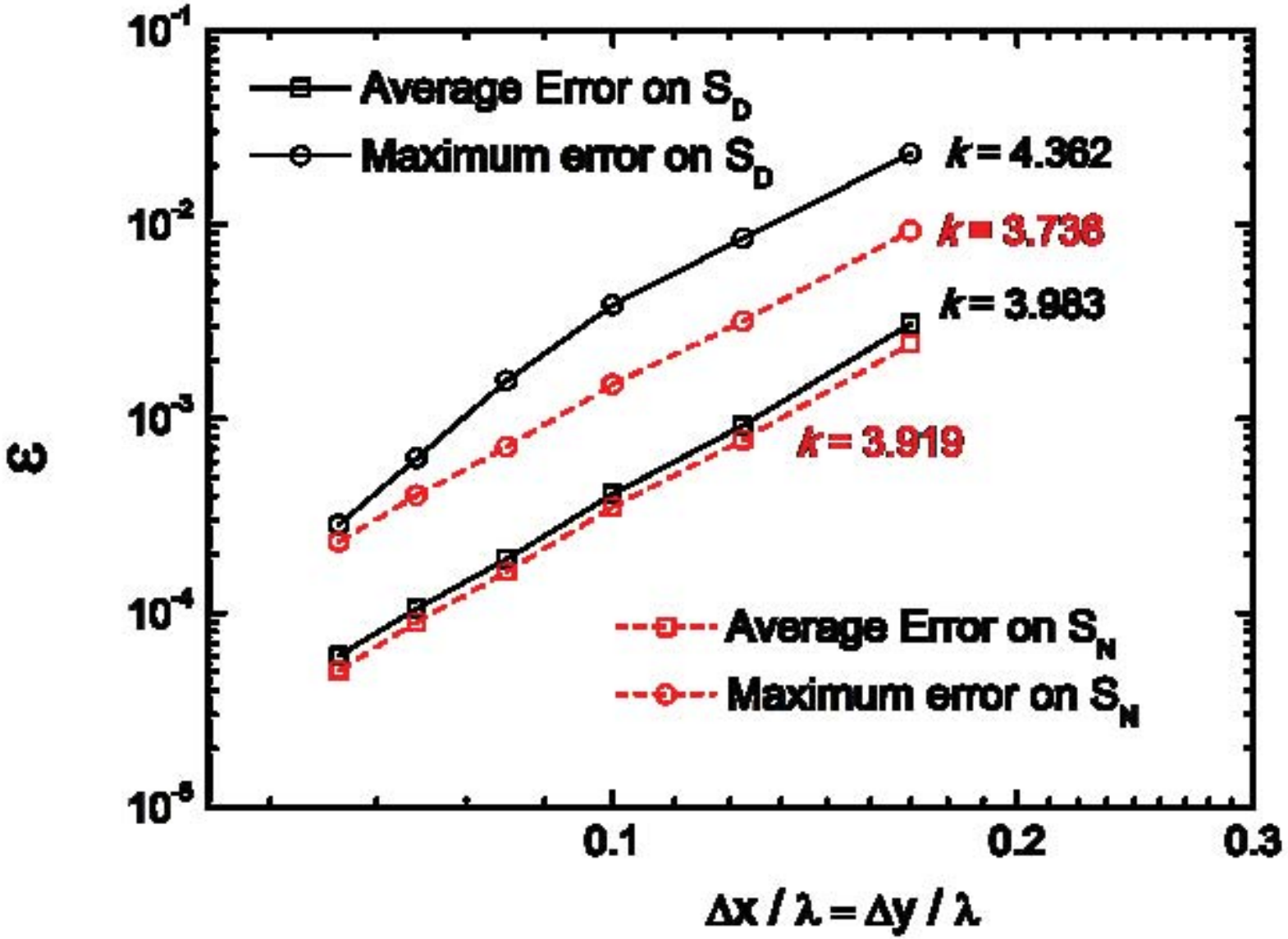

Figure 9

Click here to download high resolution image

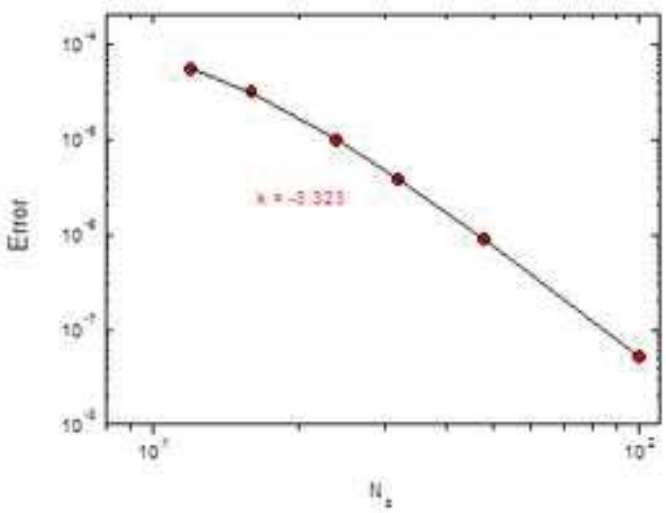

Figure 10
Click here to download high resolution image

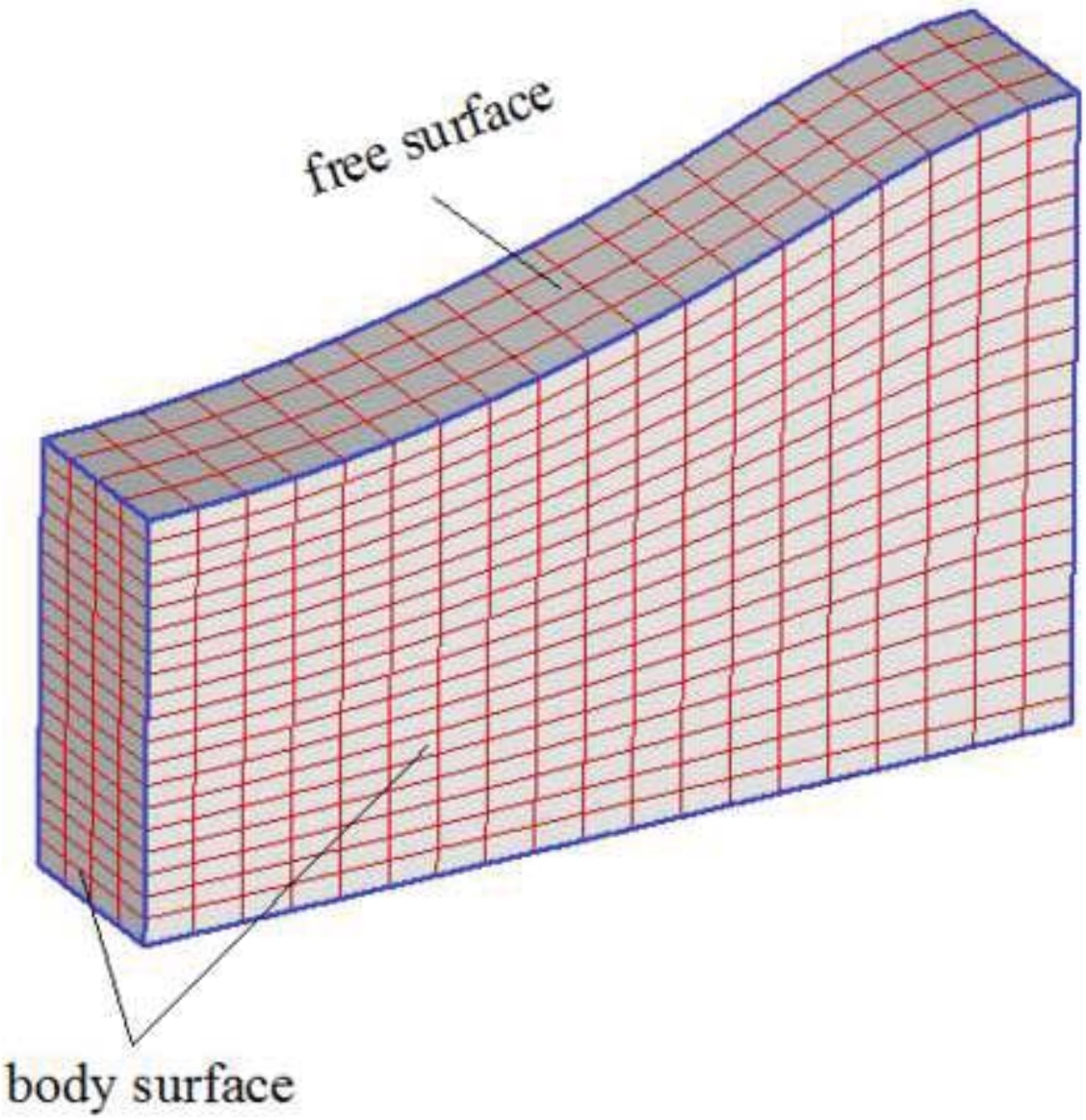

Figure 11a
Click here to download high resolution image

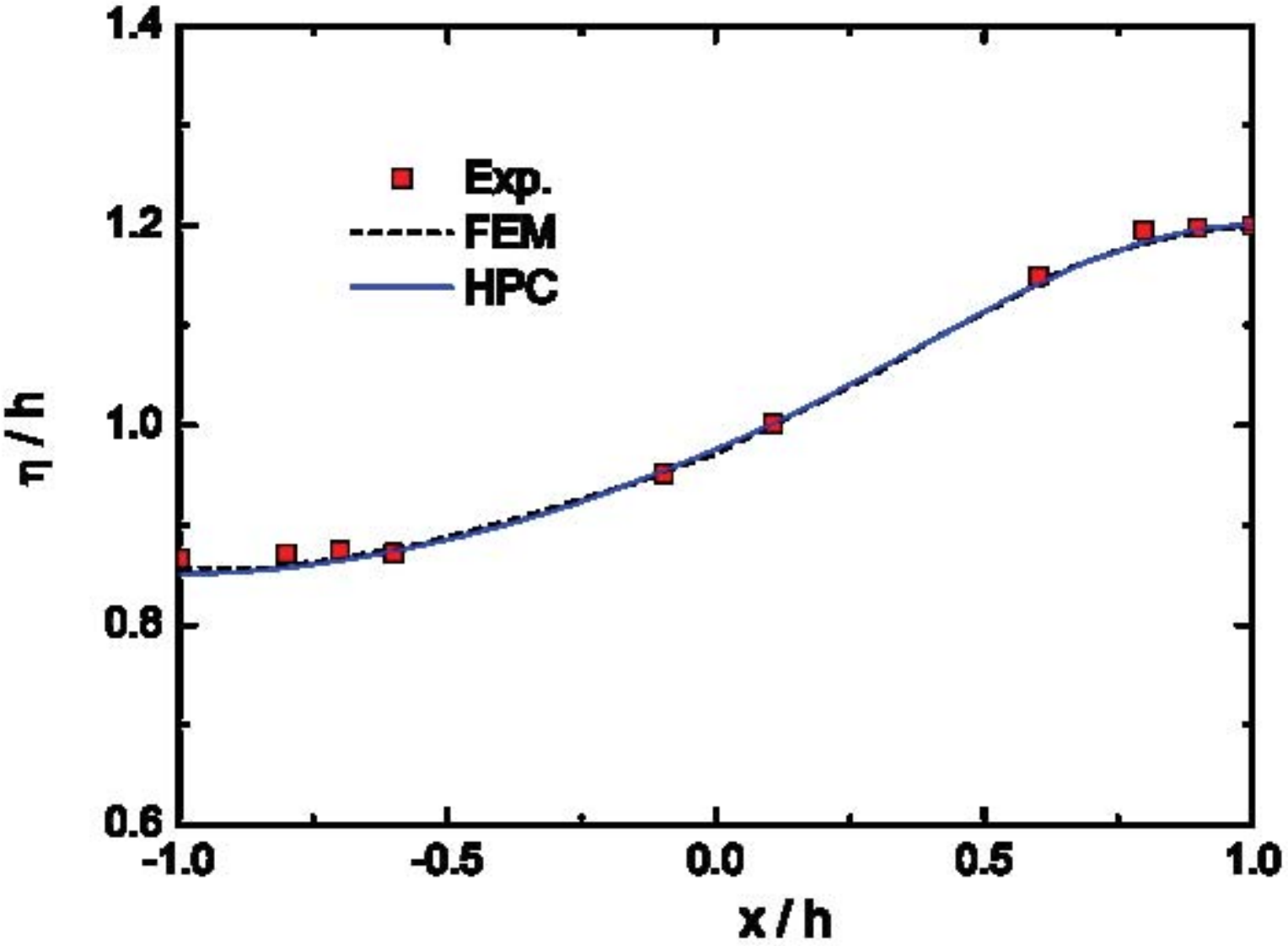

Figure 11b

Click here to download high resolution image

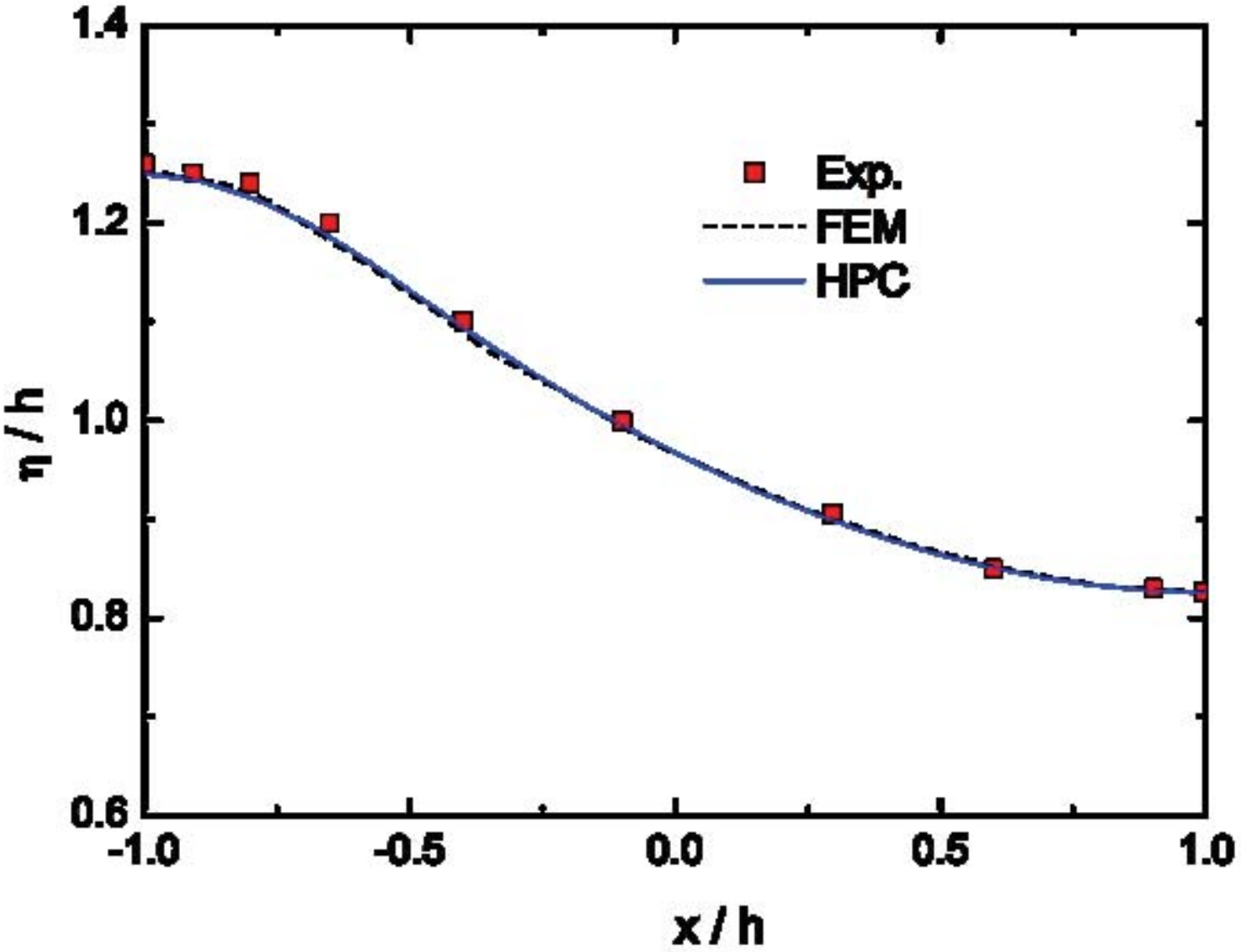

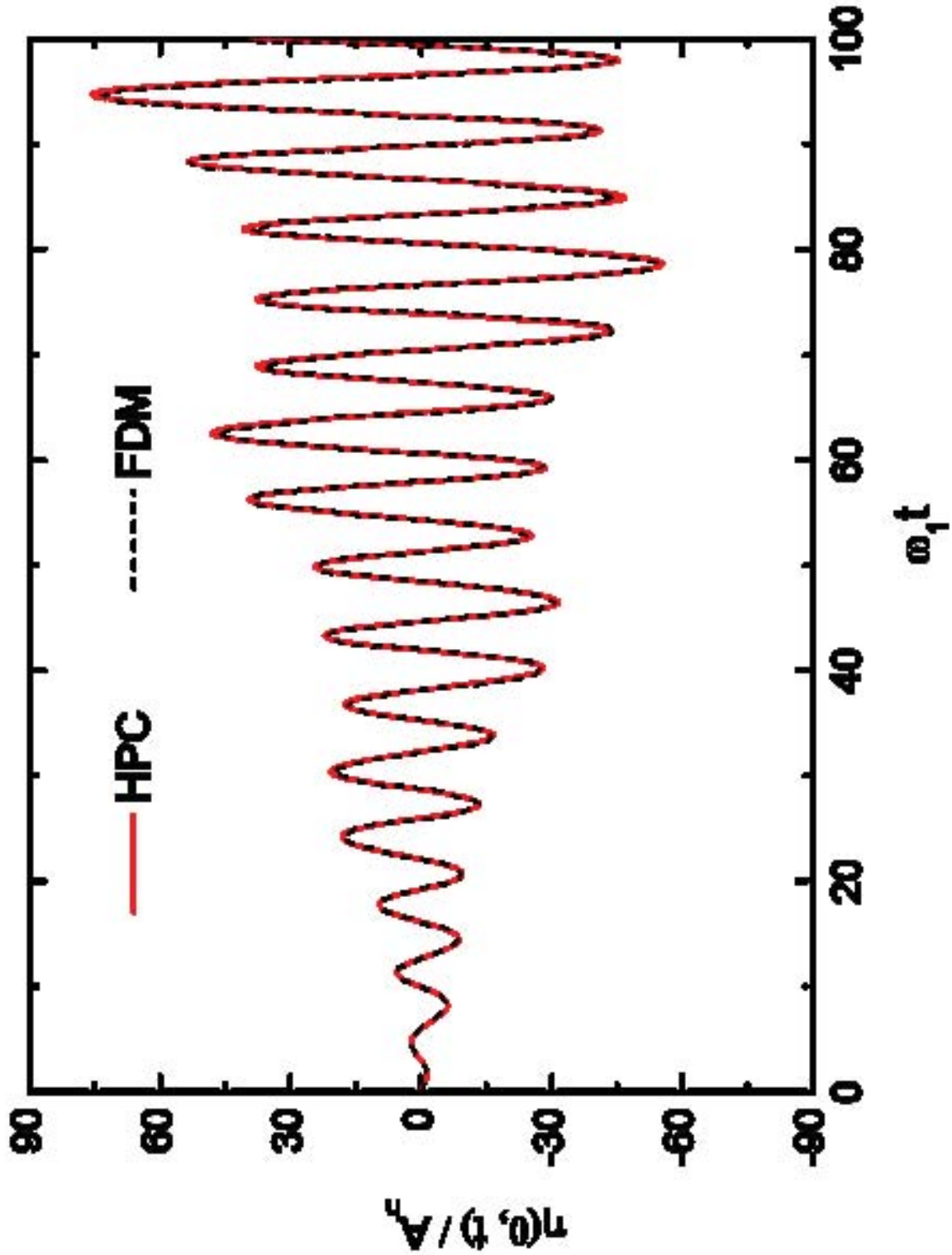

Figure 12b
Click here to download high resolution image

Figure 12a
Click here to download high resolution image

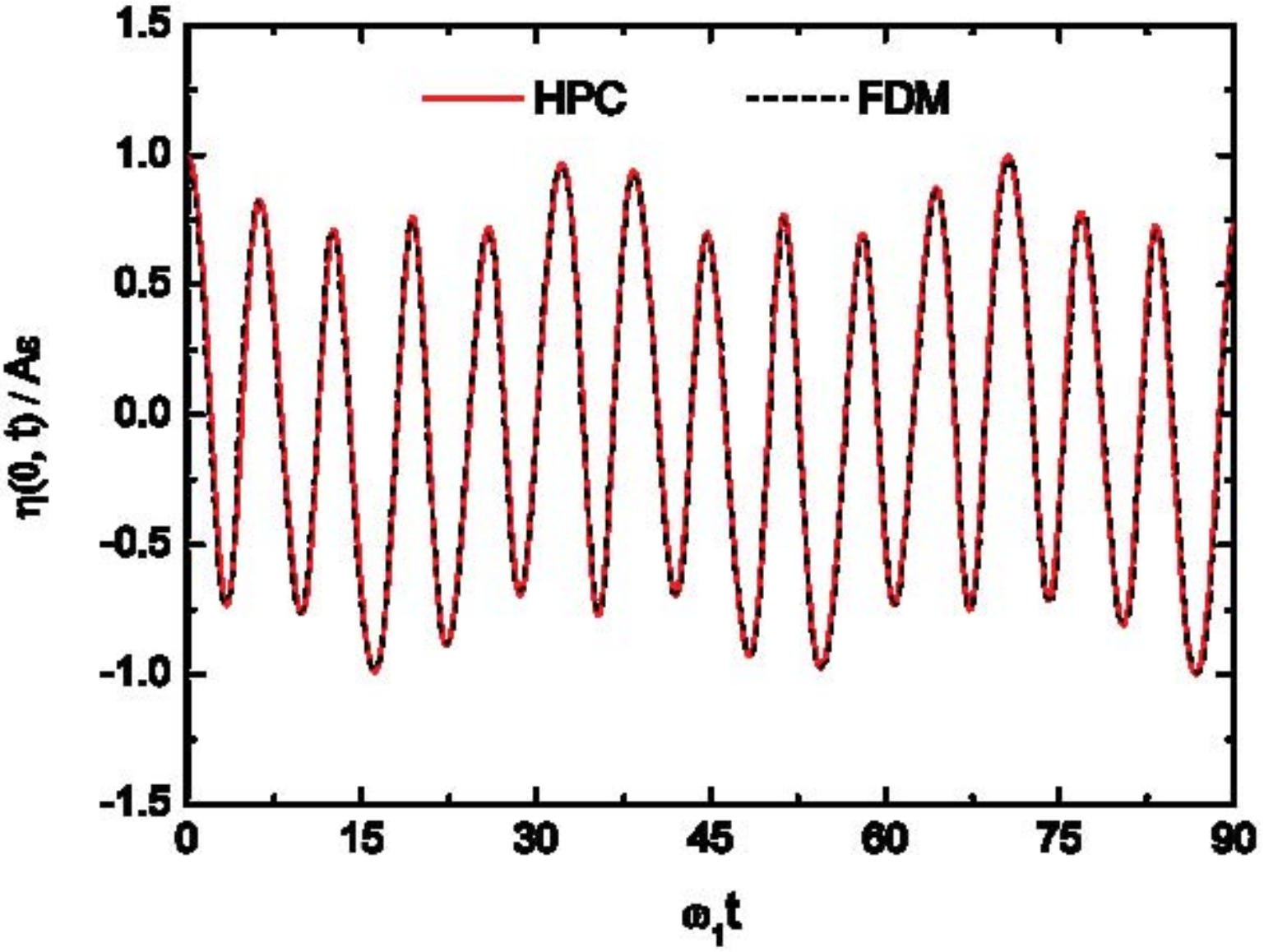

Figure 13a
Click here to download high resolution image

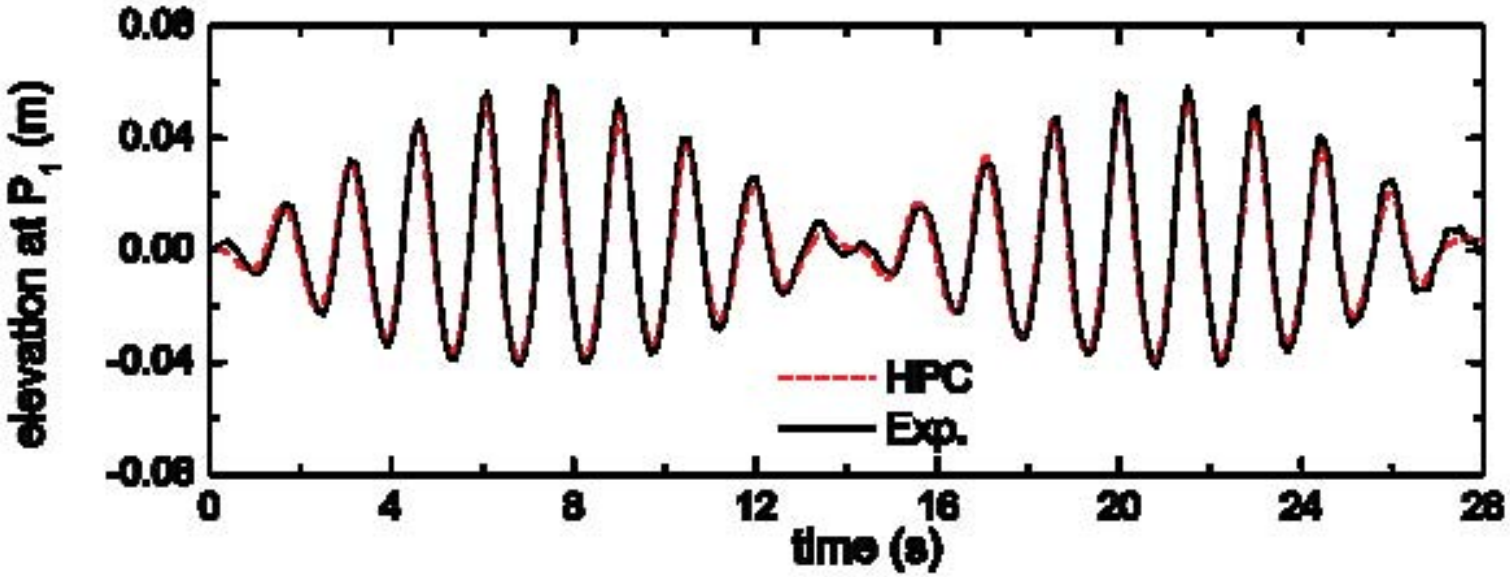

Figure 13b
Click here to download high resolution image

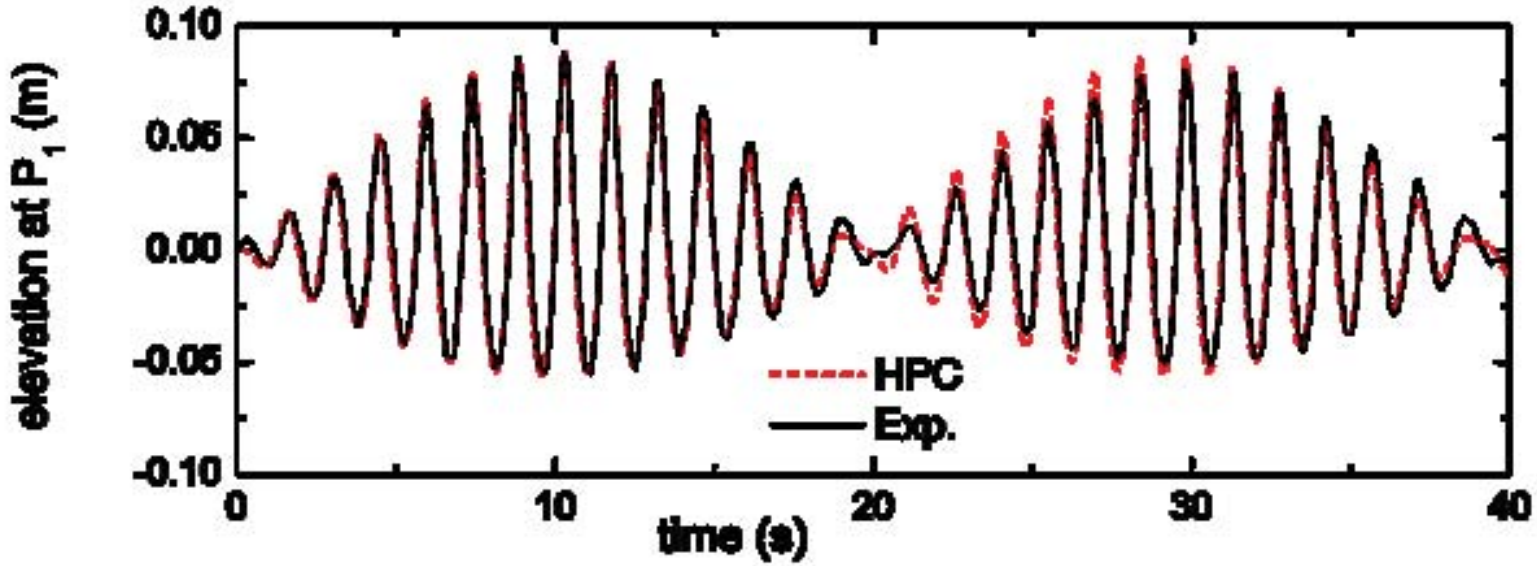

Figure 14
Click here to download high resolution image

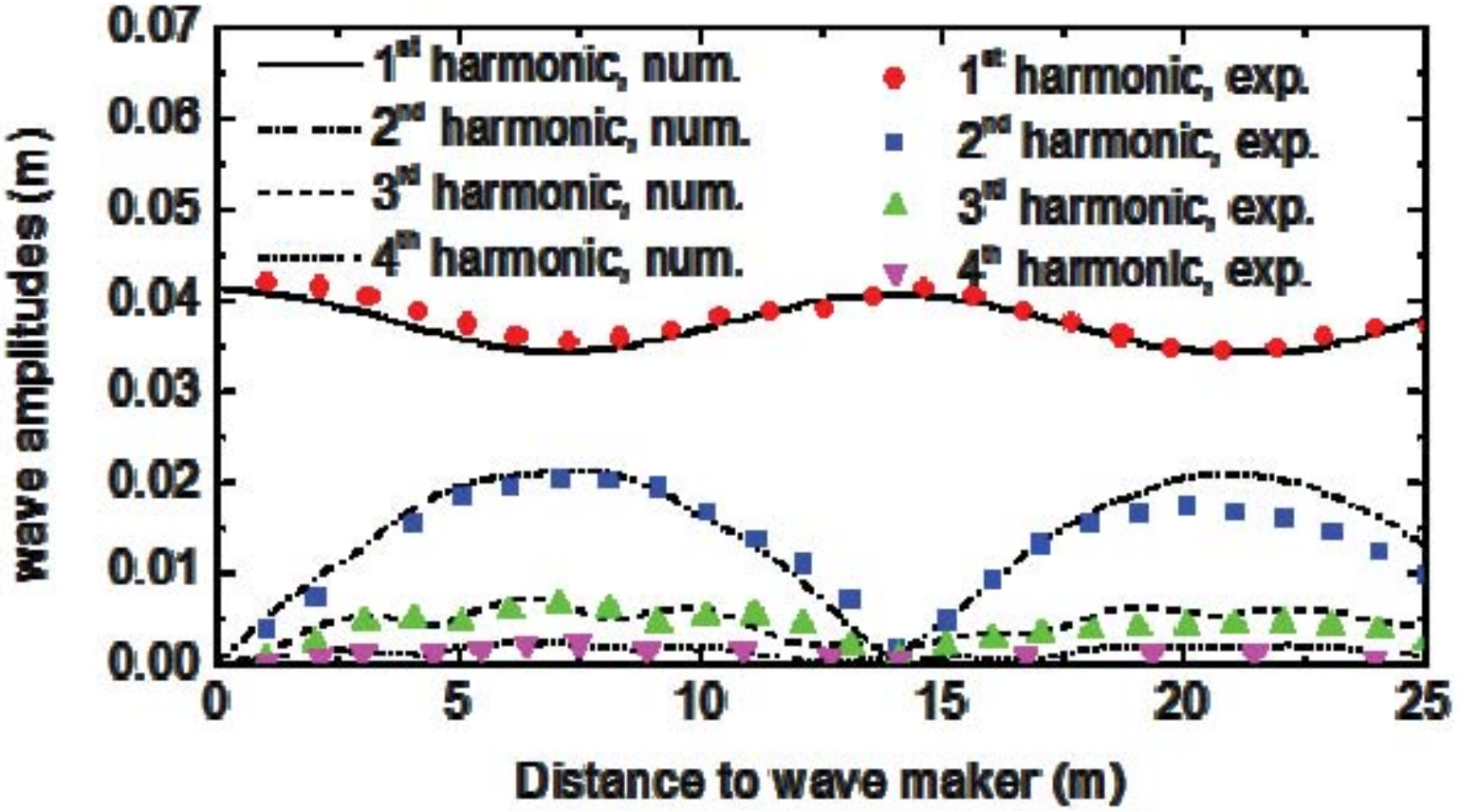

Figure 15

Click here to download high resolution image

Figure 16
Click here to download high resolution image

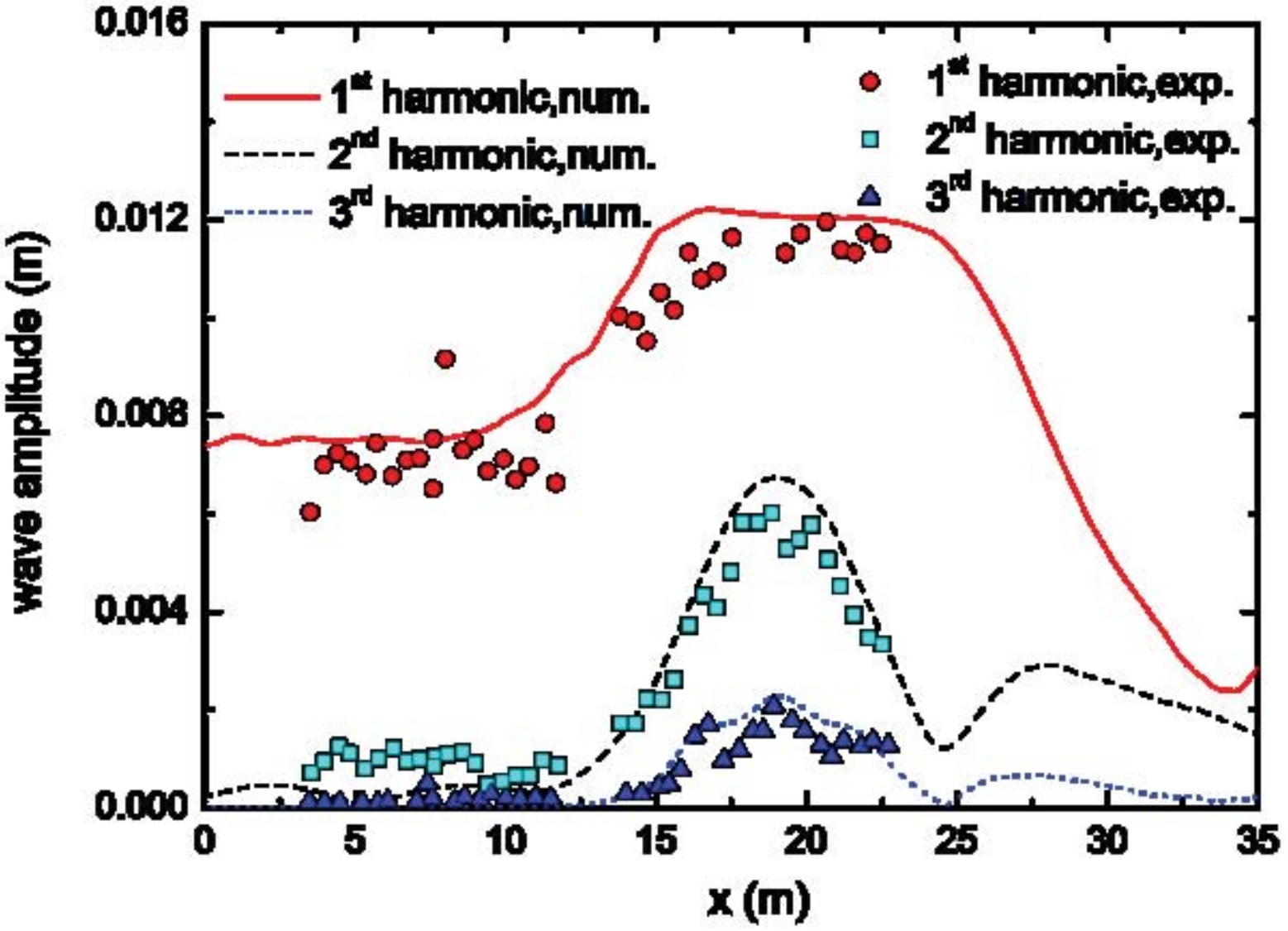

Figure 17
Click here to download high resolution image

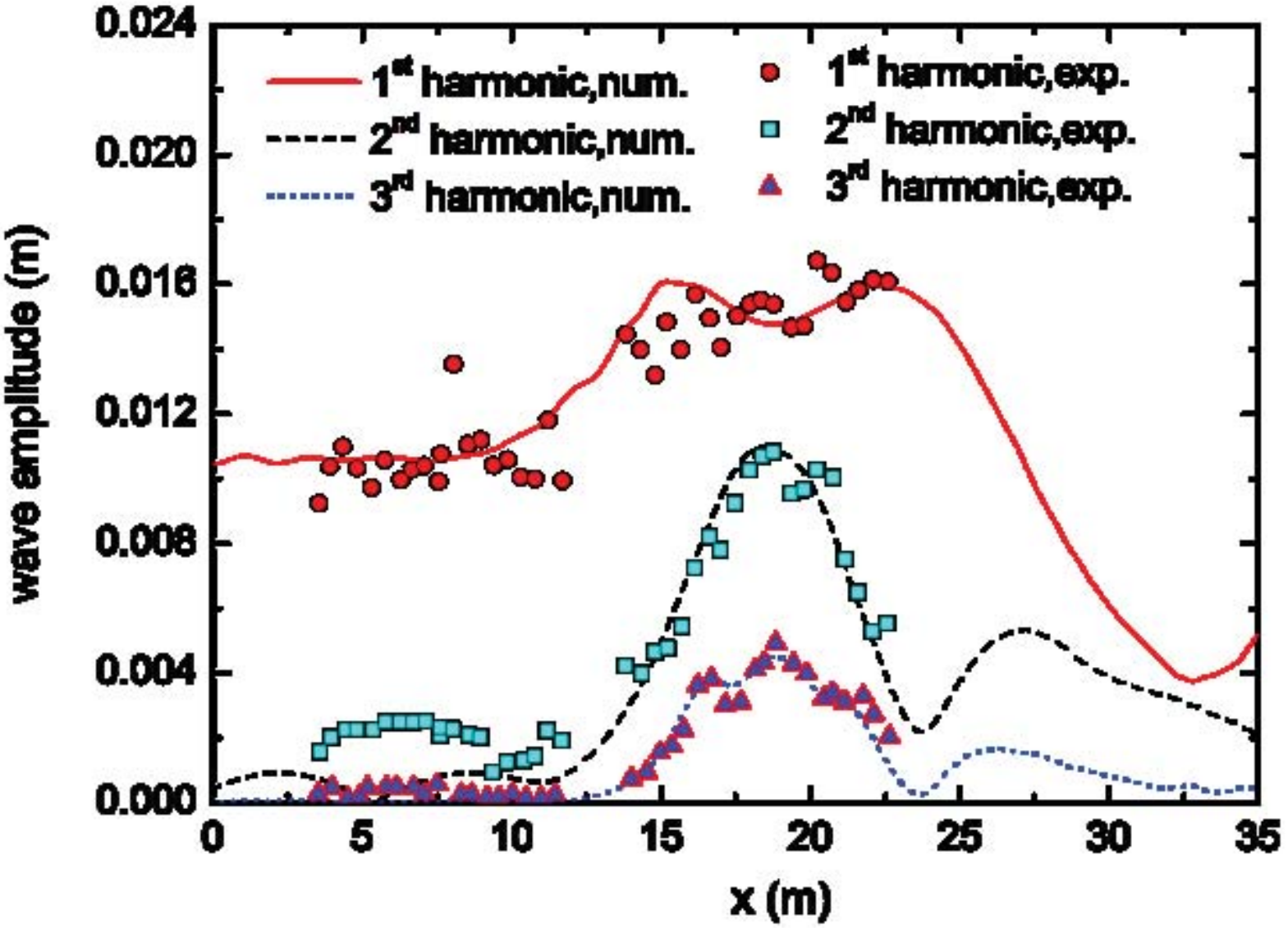

Figure 18

Click here to download high resolution image

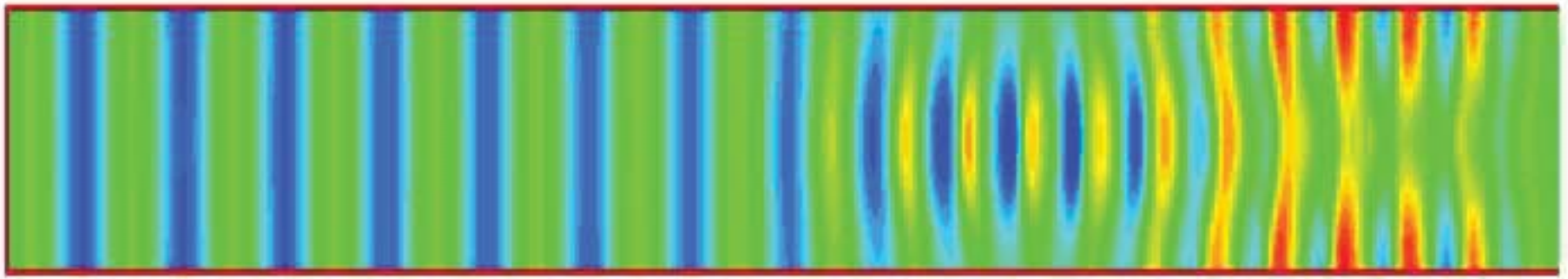

Figure 19

Click here to download high resolution image

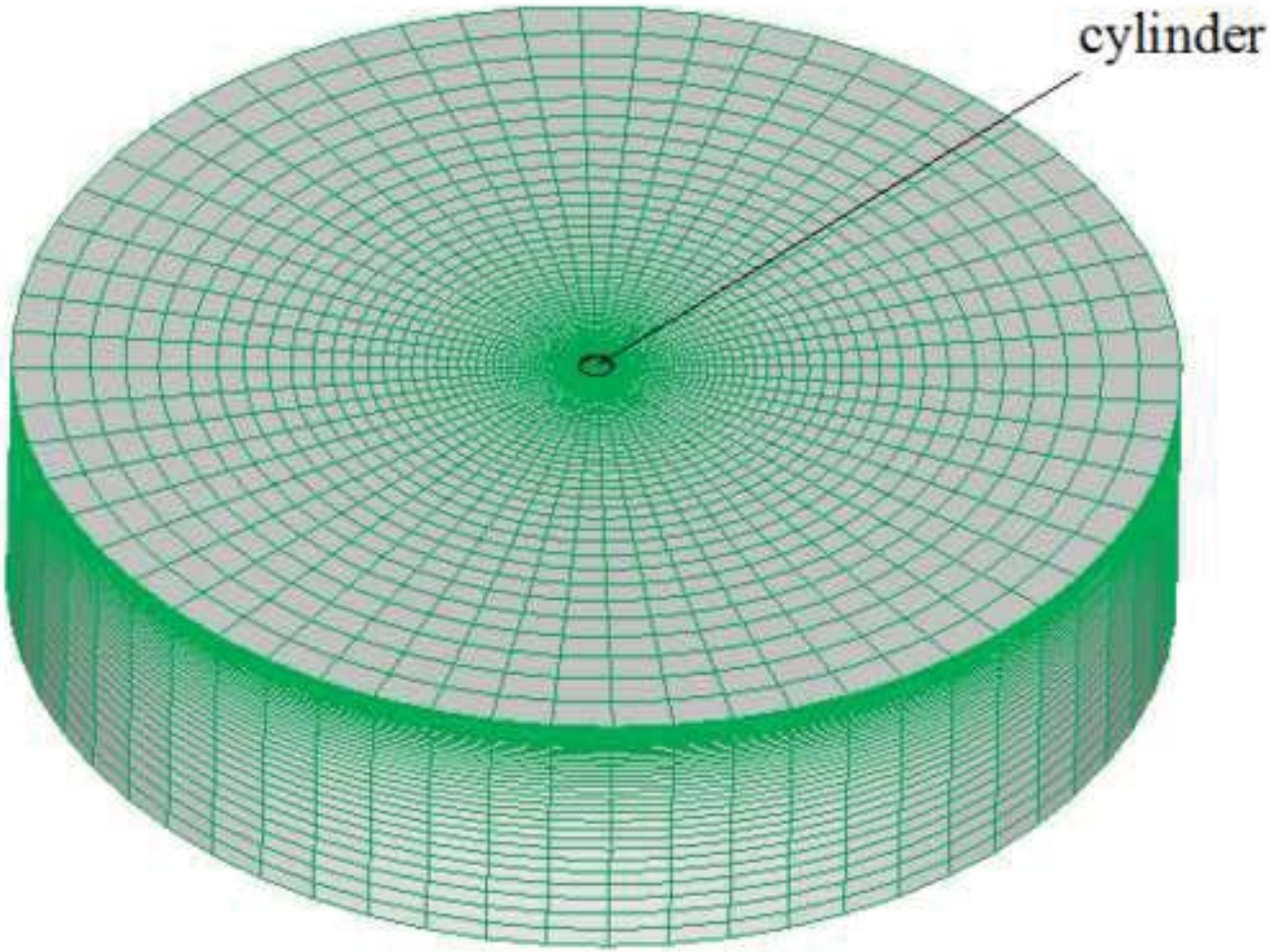

Figure 20a
Click here to download high resolution image

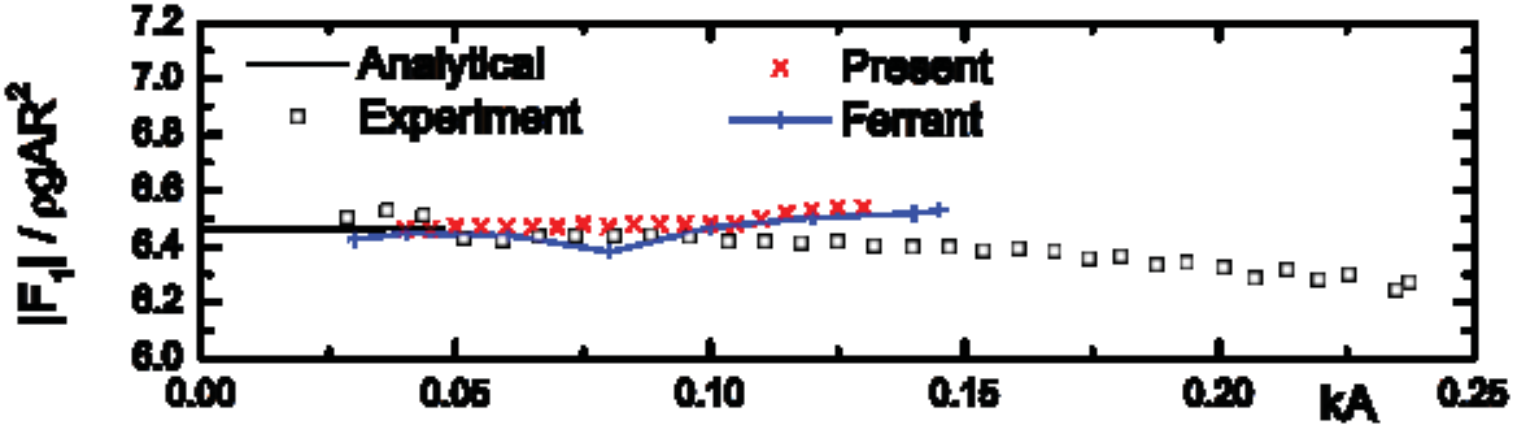

Figure 20b
Click here to download high resolution image

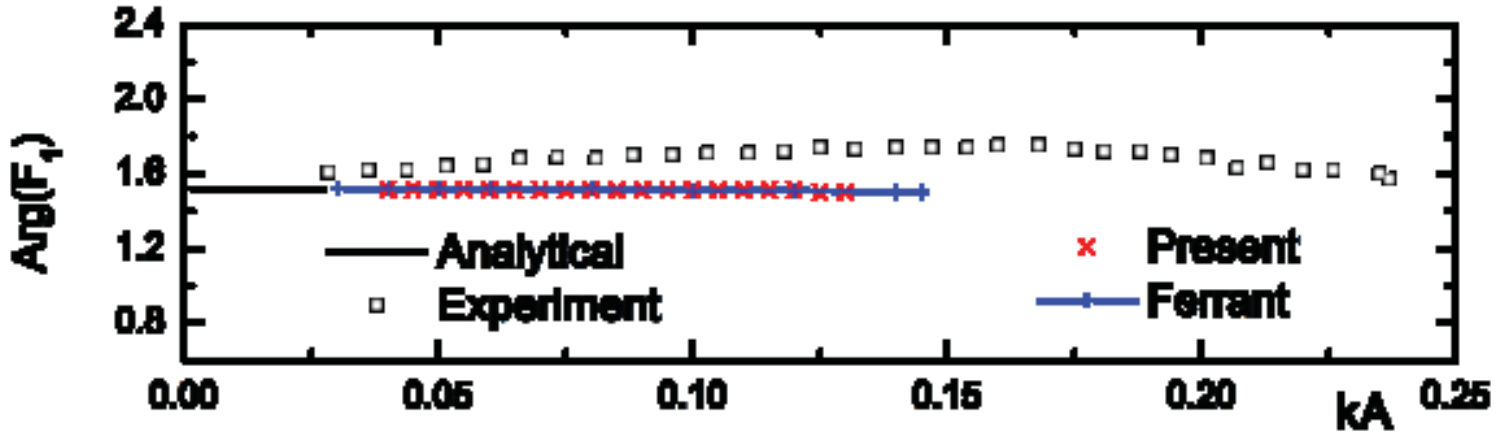

Figure 21a
Click here to download high resolution image

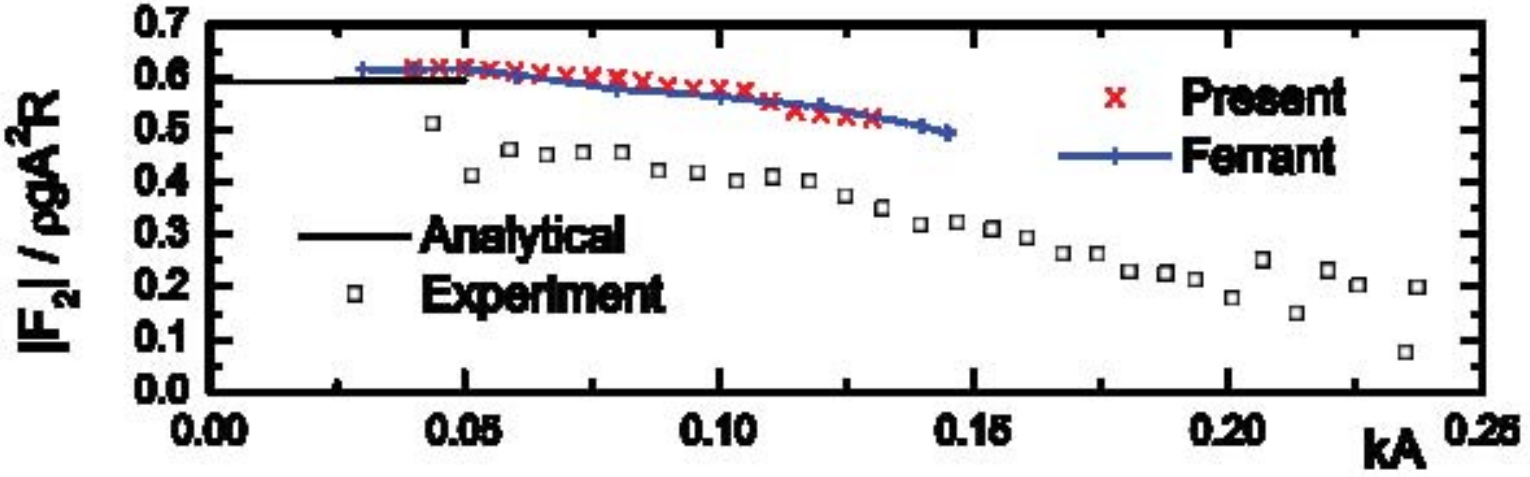

Figure 21b

Click here to download high resolution image

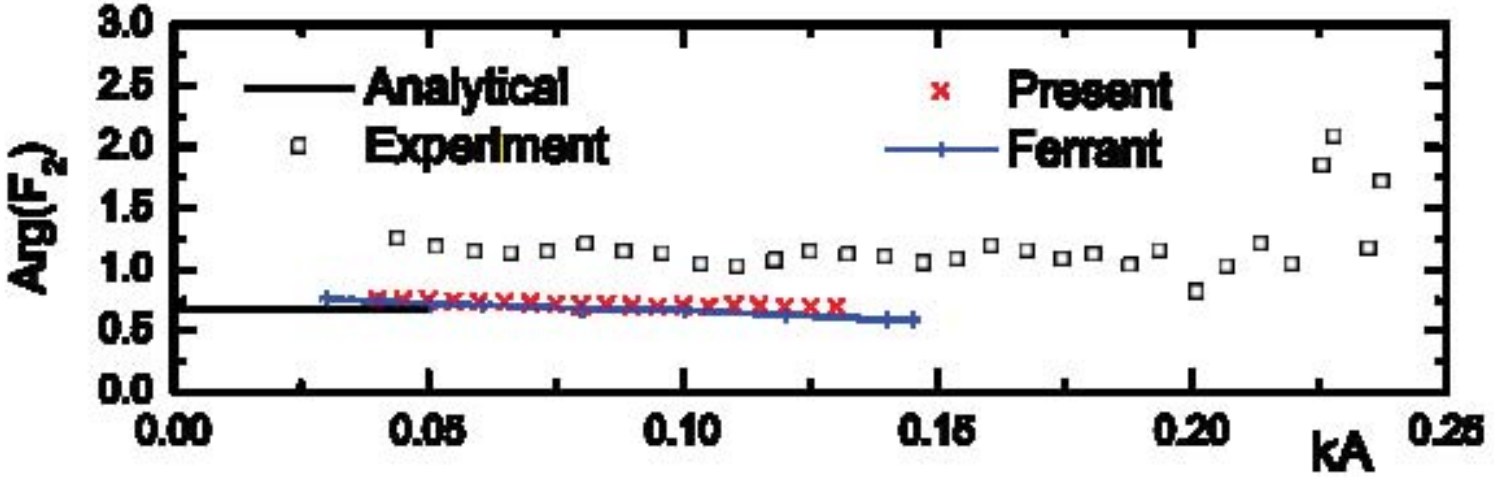

Figure 22a
Click here to download high resolution image

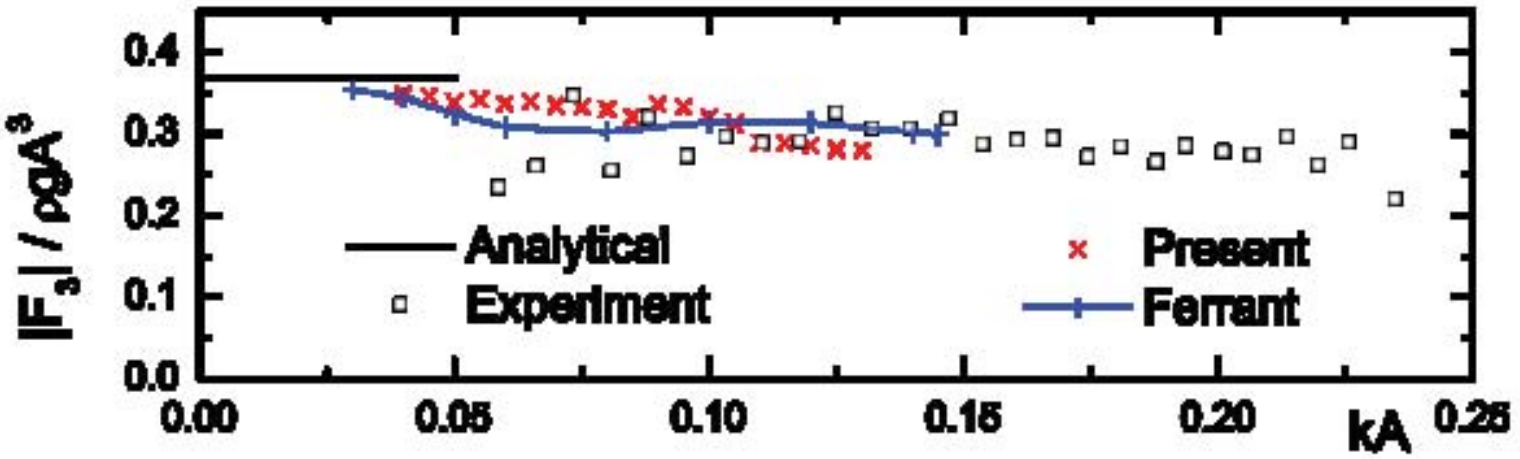

Figure 22b
Click here to download high resolution image

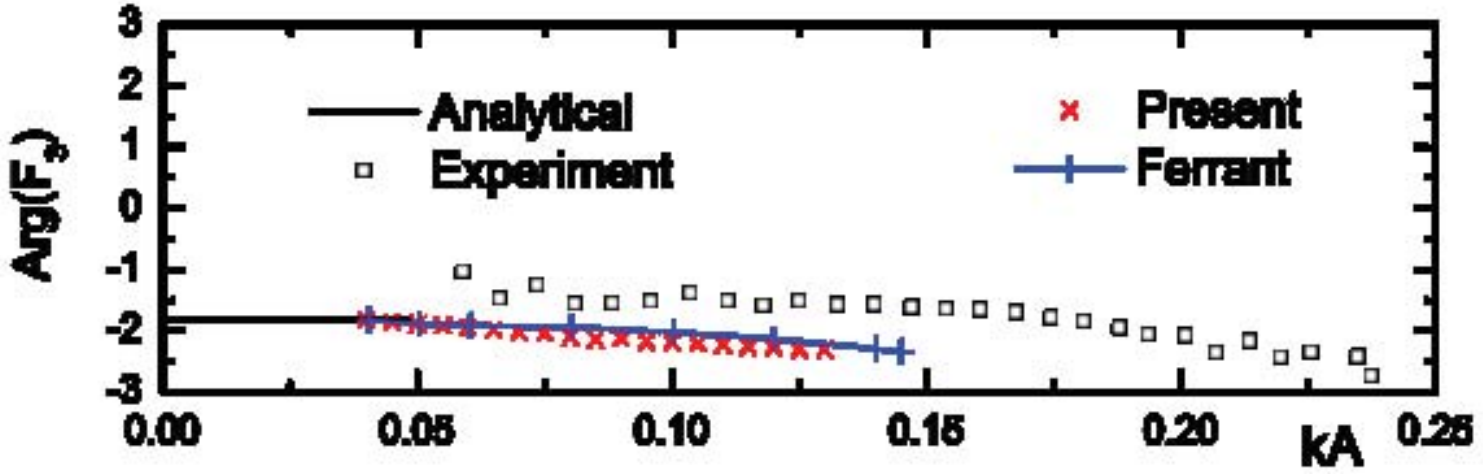

Figure 23a
Click here to download high resolution image

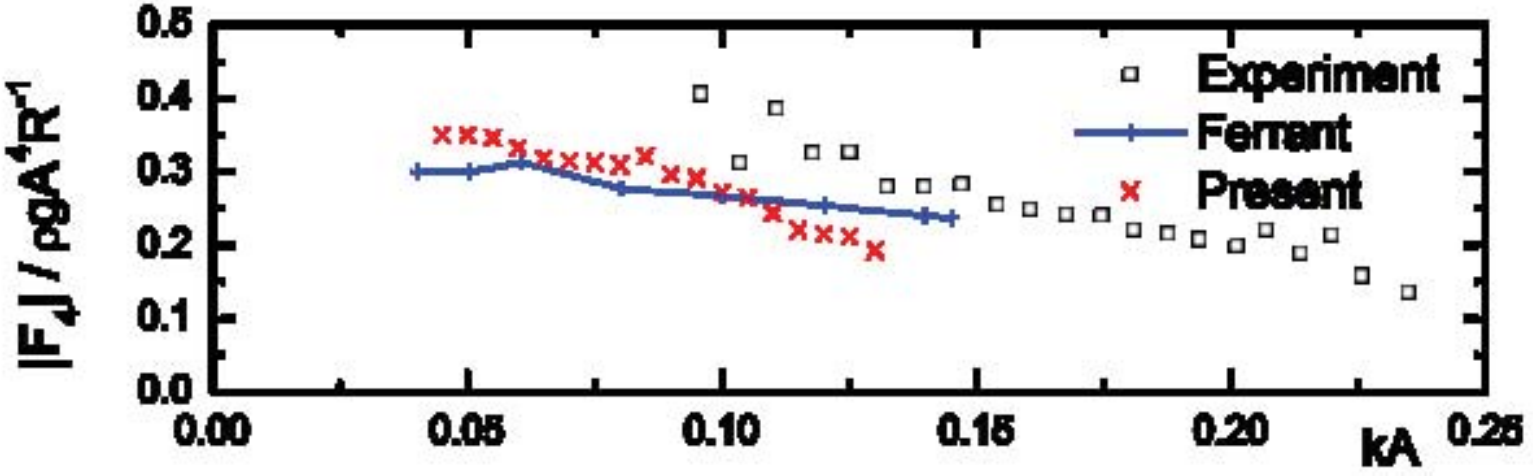

Figure 23b
Click here to download high resolution image

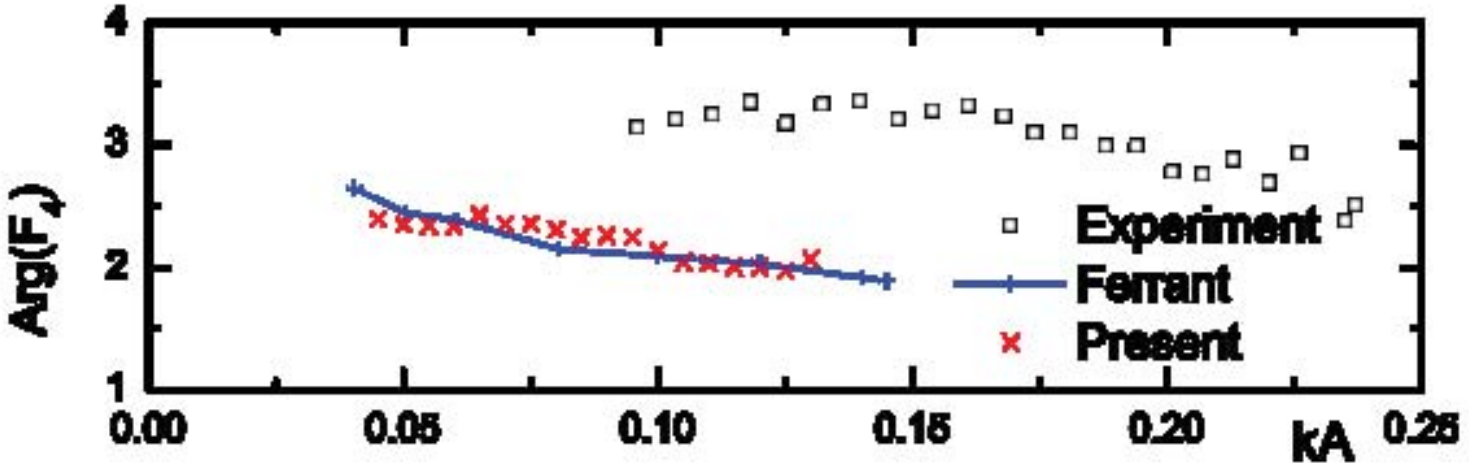

Tables

Table 1. The experimental characteristics and wave parameters

Trial	*h (m)*	*e (m)*	*T (s)*	*α*	*β*	U_r
A	0.4	0.078	2.5	0.105	0.084	14.9